frontiers | Frontiers in Earth Science

TYPE Original Research
PUBLISHED 22 May 2024
DOI 10.3389/feart.2024.1376492

OPEN ACCESS

EDITED BY
Nick Varley,
University of Colima, Mexico

REVIEWED BY
Tomohisa Tamura,
West Japan Engineering Consultants Inc., Japan
Karoly Nemeth,
Institute of Earth Physics and Space Science (EPSS), Hungary

*CORRESPONDENCE
Meng Wang,
mwang@cugb.edu.cn
Tong Hou,
thou@cugb.edu.cn

RECEIVED 25 January 2024
ACCEPTED 18 April 2024
PUBLISHED 22 May 2024

CITATION
Su C, Wang M, Luo D and Hou T (2024), Petrological and geochemical insights into the magma plumbing system of the Daliuchong dacite eruption, Tengchong Volcanic Field, SW China.
Front. Earth Sci. 12:1376492.
doi: 10.3389/feart.2024.1376492

Petrological and geochemical insights into the magma plumbing system of the Daliuchong dacite eruption, Tengchong Volcanic Field, SW China

Chaoxing Su[1,2], Meng Wang[1,3]*, Diao Luo[1,2] and Tong Hou[1,2,4]*

[1]Frontiers Science Center for Deep-time Digital Earth, China University of Geosciences (Beijing), Beijing, China, [2]Key Laboratory of Intraplate Volcanoes and Earthquakes (China University of Geosciences, Beijing), Ministry of Education, Beijing, China, [3]Hebei Province Collaborative Innovation Center for Strategic Critical Mineral Research, Hebei GEO University, Shijiazhuang, China, [4]Institute of Mineralogy, Leibniz Universität Hannover, Hannover, Germany

The formation of highly evolved, dacitic magmas has been attributed to various processes, including crystal fractionation, partial melting of overlying crust, and/or assimilation of crustal material into an evolving magma chamber. These processes are undoubtedly primary processes involved in the formation of dacites, but they may not be the only mechanism involved in the formation of high-silica dacites. For instance, mafic magma replenishment has been proposed as an additional mechanism but has not been assessed, and thus, its role has not been well-constrained. The Daliuchong volcano is the result of one of the largest eruptive events within the Tengchong Volcanic Field (TVF) in southwest China during the Early-Middle Pleistocene. Here, we conducted detailed mineral textures, mineral chemistry, and geochemical studies on Daliuchong pyroclastic rocks to explore the pre-eruptive storage conditions and evolution processes of the magma. The Daliuchong pyroclastic rocks are dacitic in composition. The samples show porphyritic textures characterized by phenocrysts of plagioclase, amphibole, clinopyroxene, orthopyroxene, and Fe-Ti oxides. Additionally, two distinct types of glomerocryst are identified: a gabbroic glomerocryst containing plagioclase + clinopyroxene + orthopyroxene ± Fe-Ti oxides assemblage and a dioritic glomerocryst containing plagioclase + amphibole ± pyroxene ± Fe-Ti oxides assemblage. Both phenocryst and glomerocryst show rich micro-textures. The Daliuchong dacite exhibits bulk compositional heterogeneity. Analysis of bulk-rock data suggests that this heterogeneity may arise from both the differentiation of the dacite itself and the injection of mafic magma. The compositional similarity between the Daliuchong dacite and experimentally produced partial melts of metamorphic basalt supports that the Daliuchong dacite was predominantly formed through the partial melting of the mafic lower crust. Thermobarometry estimation indicates that clinopyroxenes with high Mg# crystallized at 560–870 MPa, whereas amphibole and clinopyroxenes with low Mg# crystallized at 185–300 MPa. Based on the observed phase relations and the calculated crystallization conditions, we propose that during the differentiation of the Daliuchong

dacite, heterogeneous dacitic magma formed by partial melting accumulated in a deep magma reservoir (21–32 km) before subsequently ascending toward shallower depths. Crystallization of plagioclase, amphibole, Fe-Ti oxides, and small amounts of pyroxene and apatite occurred at a shallower depth (7–10 km). The presence of coarse-sieve texture, fine-sieve texture, and oscillatory zoning with high amplitude in plagioclase suggests intermittent injection of mafic magma into the shallow magma reservoir, with the eruption of dacitic magma occurring after the final mafic magma replenishment. The petrological evidence above advocates that primitive magma replenishment could have been involved in the formation and triggered the eruption of dacite in the Daliuchong volcano.

KEYWORDS

Tengchong, Daliuchong, volcano, dacite, pre-eruptive processes, plumbing system

1 Introduction

Understanding the evolution and pre-eruptive storage conditions of magma in the crust is crucial for exploring the magma plumbing system. Magmatic storage conditions, such as pressure, temperature, volatile content, and redox condition, not only influence the crystallization sequence (e.g., Rutherford and Devine, 1988; Arce et al., 2006; Knafelc et al., 2020), mineral phase abundance (Rutherford and Devine, 1988; Arce et al., 2006; Knafelc et al., 2020), and mineral composition (e.g., Johnson and Rutherford, 1989; Prouteau and Scaillet, 2003; Holtz et al., 2005) in magmas but also play a significant role in determining eruptive types (e.g., Degruyter et al., 2017; Cassidy et al., 2018; First et al., 2021). Dacitic magmas are predominantly associated with explosive eruptions and catastrophic events due to their characteristics of high viscosity and volatile content, as exemplified by notable volcanoes such as Mount St. Helens in Washington, USA (Sigurdsson et al., 1985), Malinche in Mexico (Espinosa et al., 2021), Pinatubo in Philippines (Scaillet and Evans, 1999), and Santorini in Greece (Cottrell et al., 1999; Cadoux et al., 2014). Nevertheless, the petrogenesis of dacite remains contentious, and several distinct models have been proposed: 1) effective mixing of rhyolitic and basaltic magmas (e.g., Banaszak, 2014; Millet et al., 2014; Gao et al., 2015); 2) crystal fractionation of basaltic or andesitic magmas (Grove et al., 2005; Arce et al., 2006; Haase et al., 2006); 3) partial melting of the lower crust (e.g., Wolf and Wyllie, 1994; Rapp and Watson, 1995; Winther, 1996; Springer and Seck, 1997; Nakajima and Arima, 1998; Yamamoto, 2007); 4) crustal contamination of mafic magmas (Arce et al., 2006; Cheng et al., 2020). Hence, a comprehensive understanding of pre-eruptive storage conditions and evolution processes of dacitic magmas is essential, especially for active volcanoes.

The Tengchong Volcanic Field (TVF) in Southwest China hosts 68 active volcanoes. Among them, the Daliuchong dacitic volcano is considered the source of one of the largest eruptions during the Early to Middle Pleistocene epoch (Li et al., 2014a). This study presents a detailed investigation of the textures and compositional zoning of both phenocrysts and glomerocrysts in the pyroclastic rocks of Daliuchong, aiming to elucidate the complex magmatic processes that occurred during magma storage and ascent to the surface. Additionally, this research will provide new insights into the genesis of intermediate-acidic magmas during the Early to Middle Pleistocene period in the TVF.

2 Geologic setting

The TVF, situated in southwest Yunnan Province and the southeast Tibetan Plateau, stands as one of the primary active volcanic systems in southwest China (Figure 1). Tectonically, it lies within the eastern part of the arcuate tectonic belt of Burma (Jiang et al., 2003), bordered by Burma to the west, the Gaoligong fault to the east, and the Ruili-Mandalay fault to the south (Huang et al., 2013). Since the Cenozoic era, the collision between the Indian and Eurasian plates has resulted in compression of the Tibetan Plateau block in a north-south (NS) direction, generating an east-west strip uplift within the plateau and causing extension at both ends. Consequently, a nearly east-west compressive stress field has developed in the western Sichuan and Yunnan regions. Under this stress field, the Tengchong area exhibits a tectonic pattern primarily oriented in a NS direction (e.g., Jiang et al., 1998; Wang, 1999; Zhang et al., 2012a). The collision between the Indian and Eurasian plates has resulted in significant tectonic deformation, accompanied by extensive volcanic and hydrothermal activities (Cheng et al., 2020). Volcanic activity is predominantly controlled by north-south trending faults, resulting in the NS distribution of volcanic vents along these faults (Jiang et al., 1998; Zhang et al., 2012b; Li et al., 2014b). The seismic observations indicate that the crustal thickness of the TVF ranges from 35 to 40 km (Xu et al., 2017). The TVF exposes Proterozoic to Quaternary strata. Specifically, the Proterozoic strata predominantly consist of metamorphic rocks of the Gaoligong Group, with upper layers comprising schist and leptynite and lower layers primarily composed of gneiss, leptynite, and amphibolite (Yu, 2016). Late-Paleozoic to Mesozoic sedimentary cover is dominated by carbonate rocks, interspersed with intermittent clastic rocks. Neogene to Quaternary strata consist mainly of fluvial-lacustrine clastic sedimentary rocks (Wan et al., 2018).

The volcanic activity of the TVF is temporally concentrated during the Pliocene-Holocene periods, reaching its climax in the Late Pleistocene when it formed numerous cinder cones (Li and Zhang, 2011), and it exhibits clear multi-stage eruption histories. Previous geochronological studies, along with fieldwork

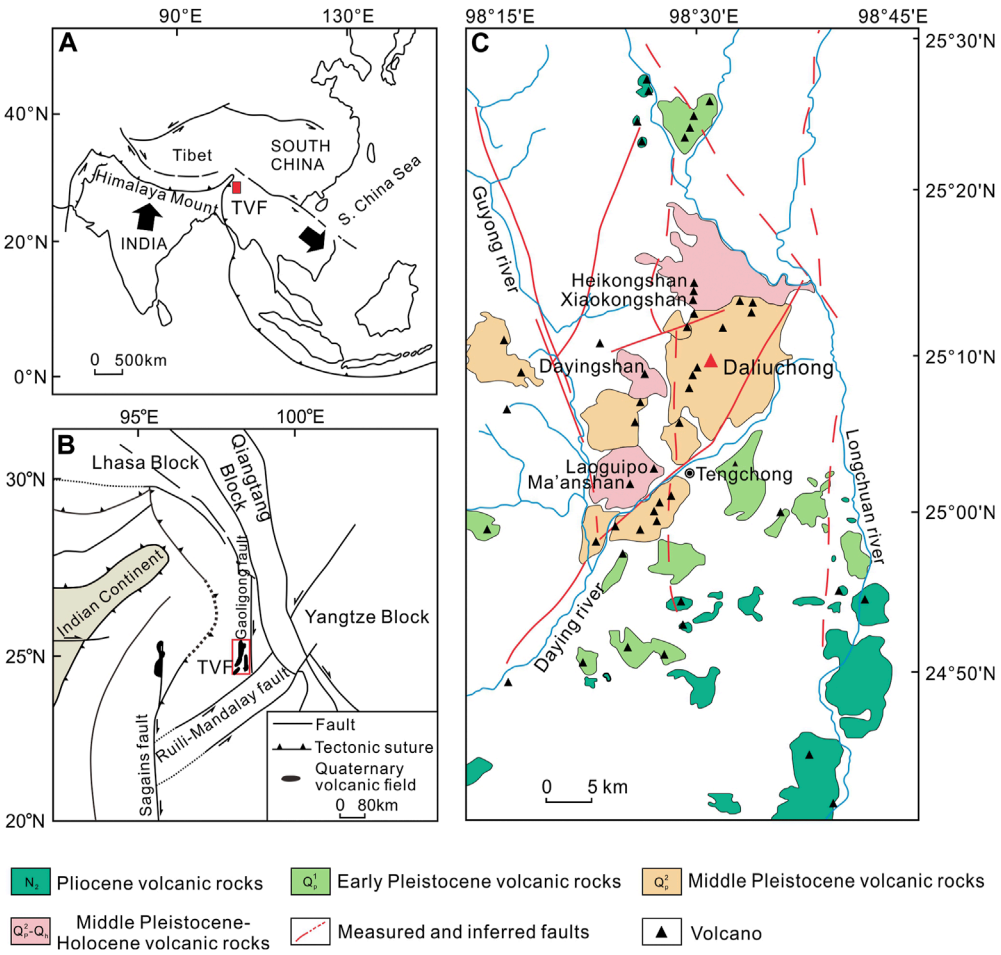

FIGURE 1
(A) Tectonic location of the TVF (modified after Tapponnier et al., 1990). **(B)** Tectonic setting of the TVF (modified after Li et al., 2020). **(C)** Map showing the volcano distribution in the TVF (modified after Yu et al., 2022).

on Tengchong volcanic activity, divided the eruptive sequence of the Tengchong volcanic group during the Quaternary into four subsequences: the Pliocene, Early Pleistocene, Middle Pleistocene, and Middle Pleistocene–Holocene epochs (Yu et al., 2022 and references therein). The volcanic activity in the TVF exhibits the characteristic of becoming progressively younger from the periphery toward the center (Li and Zhang, 2011; Li et al., 2014a). Specifically, during the Pliocene (N_2) epoch (3.83–2.71 Ma), volcanic activity was primarily concentrated in the southeastern part of the TVF, with some occurring in the northern part, producing mainly basalt and trachybasalt. In the following early Pleistocene (Q^1_P) epoch (1.99–0.84 Ma), volcanic activity shifted from the periphery, such as the southeast, toward the central region, exhibiting a wide distribution and consisting predominantly of dacite and trachyandesite. Later, during the Middle Pleistocene (Q^2_P) (0.72–0.13 Ma), volcanic activity continued to be centered in the central part of the TVF, characterized by dacitic eruptions. Eventually, during the Middle Pleistocene–Holocene (Q^2_P-Q_h) epoch (<0.078 Ma), volcanic activity diminished in scale, primarily concentrated in several locations, including Heikongshan, Ma'anshan, Dayingshan, Laoguipo, and Xiaokongshan (Figure 1). The erupted products during this period primarily consisted of basaltic trachyandesite, basaltic trachyte, and trachyandesite. Notably, recent K-Ar dating results for the Daliuchong volcano yielded ages of 0.51–0.56 Ma (Li et al., 2020). When considering these dating results alongside field observations, Daliuchong is classified as an Early to Middle Pleistocene volcano within the TVF (Li et al., 2020).

3 Volcano geology

The Daliuchong volcano, the highest peak in the TVF, reaches an altitude of 2783 m (Li et al., 2014b) with a volcanic cone height of 973 m (Zhang et al., 2012a). It has undergone multiple eruptions throughout the Pleistocene (Li et al., 2020). The volcanic cone is predominantly comprised of a thick layer of dacitic pyroclastic deposits, including welded tuff, agglomerate, and volcanic breccia, with sporadic lavas occurrence on its upper parts or flanks (Li et al., 2014a). A volcanic conduit measuring up to 100 m in diameter is situated 100 m south of the summit. The thickness of dacitic lava and pyroclastic deposits exceeds several hundred meters, with explosive volcanic products covering an area of nearly 100 km^2 (Li et al., 2014b; Li et al., 2020).

TABLE 1 Modal mineral abundances (vol%) of representative samples from the Daliuchong pyroclastic rocks.

Sample name	Pl	Amp	Cpx	Opx	Oxi	Ph
DLC-2-1	15.2	3.2	0.1	0.2	0.1	18.8
DLC-2-2	11.8	2.7	0.1	0.2	0.2	15
DLC-2-6	15.6	5.3	0.3	0.5	0.2	21.9
DLC-4-1	12.1	3.3	2.1	2.5	0.2	20.2
DLC-4-3	8.6	2.2	0.6	0.6	0.5	12.5
DLC-4-4	10.7	4.4	1.5	2.1	0.5	19.2

Abbreviations: Pl, plagioclase; Amp, amphibole; Cpx, clinopyroxene; Opx, orthopyroxene; Qxi, Fe-Ti oxides; Ph, phenocryst and glomerocryst.

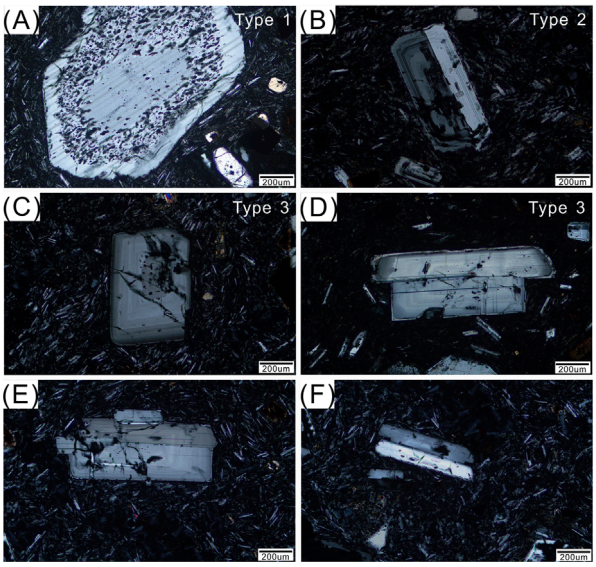

FIGURE 2
Petrographic photographs of plagioclase phenocrysts in Daliuchong dacite. **(A)** Plagioclase with coarse-sieve texture (*type 1*). **(B)** Plagioclase with oscillatory zoning (*type 2*). **(C)** Plagioclase with rounded core and normal zoning (*type 3*). **(D)** Plagioclase with rounded core, normal zoning mantle, fine-sieve margin, and subsequent overgrown rim (*type 3*). **(E)** Synneusis of plagioclase. **(F)** Swallow-tail texture of plagioclase.

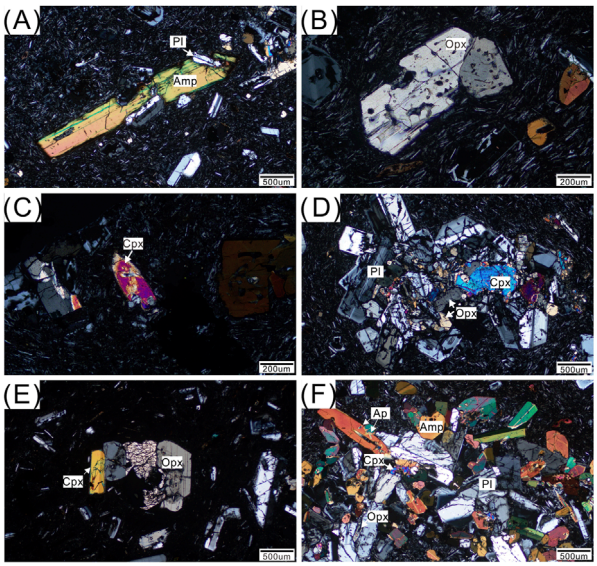

FIGURE 3
Petrographic microphotographs of mafic phenocrysts and glomerocrysts in the Daliuchong dacite samples. **(A)** Amphibole phenocryst with plagioclase inclusions. **(B)** Subhedral orthopyroxene phenocryst. **(C)** Anhedral clinopyroxene phenocryst. **(D)** Glomerocryst composed of plagioclase and pyroxene (gabbroic glomerocryst). **(E)** Glomerocryst composed of pyroxenes arranged in parallel with resorption texture. **(F)** Glomerocryst composed of plagioclase, amphibole with apatite inclusions, and pyroxene (dioritic glomerocryst).

4 Analytical methods

4.1 Electron microprobe analysis (EMPA)

Major element compositions of plagioclase, clinopyroxene, orthopyroxene, and amphibole were analyzed using an electron microprobe analyzer (EPMA; JXA-8100, JEOL) equipped with wavelength-dispersive X-ray spectrometers and one energy-dispersive X-ray spectrometer analyzer at the Institute of Geology, Chinese Academy of Geological Sciences, Beijing, China. The analyses were conducted at 15 kV accelerating voltage and 20 nA probe current, with a focused 1 μm or 5 μm beam size depending on crystal size. The analytical precision, measured relative to standard reference samples provided by SPI Supplies (USA), was better than 2%.

4.2 Bulk-rock major and trace element

Bulk-rock major element compositions (SiO_2, TiO_2, Al_2O_3, CaO, $Fe_2O_3{}^T$, MgO, MnO, Na_2O, K_2O, and P_2O_5) of six welded tuff samples were analyzed at Nanjing Hongchuang Geological Exploration Technology Service Co., Ltd., in Nanjing, China, using an inductively coupled plasma spectrometer (ICP-OES). The samples were crushed in an agate mortar and ground in an agate mill to powders of approximately 200 mesh. Loss on ignition (LOI) was determined gravimetrically after heating the samples at 1000°C for 2 h. The relative errors of the test results are less than 3%.

Bulk trace elements were analyzed using an Agilent 7900 inductively coupled plasma mass spectrometer (ICP-MS) at the Nanjing Hongchuang Geological Exploration Technology Service Co., Ltd., in Nanjing, China. For each sample, 50 mg of 200-mesh powder was dissolved in a mixture of 1.5 mL HF and 1 mL HNO_3 at 190°C for 72 h. The precision for all elements was typically better than 5% relative standard deviation (RSD).

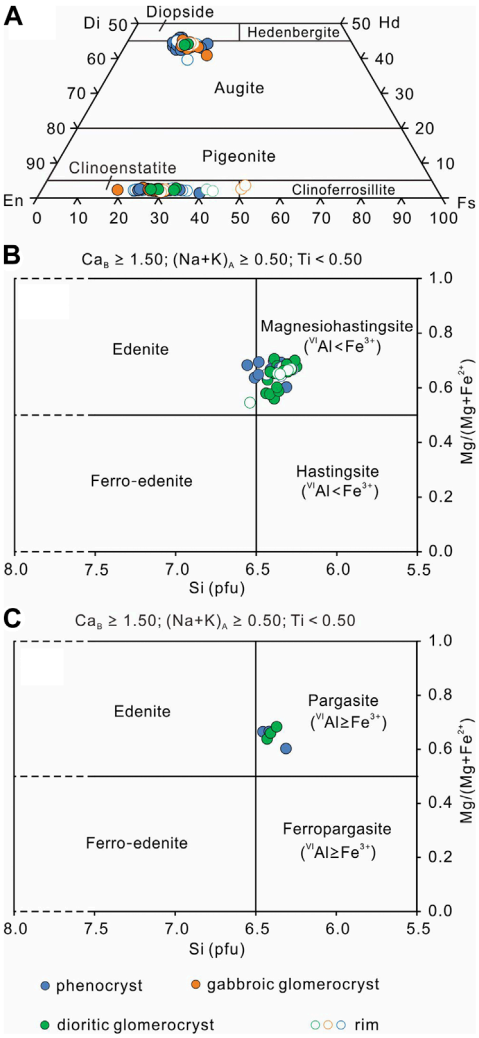

FIGURE 4
(A) Denomination of clinopyroxene and orthopyroxene in the Daliuchong samples. **(B,C)** Denomination of calcic amphibole is based on Leake et al. (1997).

4.3 Bulk Sr and Nd isotopes

Sr and Nd isotopes were analyzed at the Nanjing Hongchuang Exploration Technology Service Co., Ltd., in Nanjing, China, using a Thermo Fisher Neptune Plus MC-ICP-MS. Each powder sample was placed into a steel-jacketed high-pressure PTFE bomb with 1 mL of HNO_3 and 2 mL of HF and then dissolved at 190°C for 72 h. Subsequently, the sample was evaporated to dryness on a hotplate and reconstituted in 1 mL of concentrated HCl to form a hydrochloride medium. After evaporation, the residue was dissolved in 1 mL of 2 mol/L HCl. The separation of Sr and Nd involved the following procedure: first, a mixed-resin column was utilized to elute unwanted elements and separate REEs + HFSEs, Sr, and Pb. Second, the eluted REE + HFSE components were evaporated at 160°C and treated twice with 50 μL of 15 mol/L HCl to convert them to a hydrochloride medium. Finally, an LN Spec resin column was used to elute light rare earth elements (LREEs) and separate Nd. The $^{87}Sr/^{86}Sr$ data were normalized to a value of 0.1194 for the NIST SRM987 standard, and the $^{143}Nd/^{144}Nd$ ratios were normalized to a value of 0.7219 for the JNdi-1 standard.

5 Results

5.1 Petrography

We collected volcanic pyroclastic rock and lava samples from Daliuchong. Both exhibit massive structures, with developed vesicles in the volcanic pyroclastic rocks. The lava samples have a low phenocryst content, with predominantly darkened amphibole phenocrysts. Therefore, our study focused solely on the analysis of the volcanic pyroclastic rocks. The pyroclastic rock samples are porphyritic, containing 10–22 vol% (Table 1) of plagioclase, amphibole, orthopyroxene, clinopyroxene, and Fe-Ti oxides phenocrysts in a groundmass consisting of fine-grained quartz, plagioclase, pyroxene, and Fe-Ti oxides. Plagioclase phenocryst and glomerocrystic plagioclase account for 10–15 vol% of the rocks, ranging from 100 to 1800 μm in size, in euhedral laths. They also exhibit a variety of micro-textures, including oscillatory zoning, coarse-sieve, fine-sieve, corrosion, and mortar textures, and can be classified into three types based on their textural characteristics. The *type-1* plagioclase (Figure 2A) is characterized by large size (>1500 μm), coarse-sieve texture, and either oscillatory zoning or being unzoned, accounting for approximately 5 vol% of the plagioclase phenocrysts/glomerocrysts. The coarse-sieve texture zone often exists as a (sub-)rounded core and exhibits patchy zoning characterized by a low An [An; molar 100 ∗ Ca/(Ca+Na+K)] core surrounded by high An regions (see below for details). This zone is always demarcated by a distinct boundary from the oscillatory zoning zone. The *type-2* plagioclase (Figure 2B) also features a (sub-)rounded core and oscillatory zoning. In comparison to *type-1*, they exhibit cracks and do not display a coarse-sieve texture. This variety of plagioclase comprises approximately 30 vol% of the plagioclase phenocryst/glomerocryst population. The *type-3* plagioclase (Figures 2C, D) is characterized by a (sub-)rounded core, a normal zoning mantle, a fine-sieve margin, and a subsequent overgrown rim, comprising approximately 65 vol% of plagioclase phenocrysts/glomerocrysts. Some plagioclase grains show morphological textures such as synneusis and swallow-tailed crystal (Figures 2E, F). Moreover, amphibole is the major mafic phenocryst phase (3–6 vol%), occurring as euhedral hexagons and rectangular in shape, with sizes ranging from 150–3000 μm (Figure 3A). An opacitic border texture is largely absent in most of the amphibole phenocrysts, whilst some exhibit embayed textures. Notably, plagioclase inclusions are observed in some amphibole crystals. Trace amounts of subhedral and anhedral orthopyroxene and clinopyroxene (<5 vol%) are present in the samples (Figures 3B, C), with most of the pyroxene grains forming glomerocrysts with plagioclase grains. A few euhedral Fe-Ti oxides are also observed in our samples.

There are two types of glomerocryst found in our samples: 1) Assemblages of plagioclase + orthopyroxene + clinopyroxene ± Fe-Ti oxides (gabbroic glomerocryst) (Figure 3D), ranging in size from 2 mm to 6 mm, and mainly characterized by euhedral

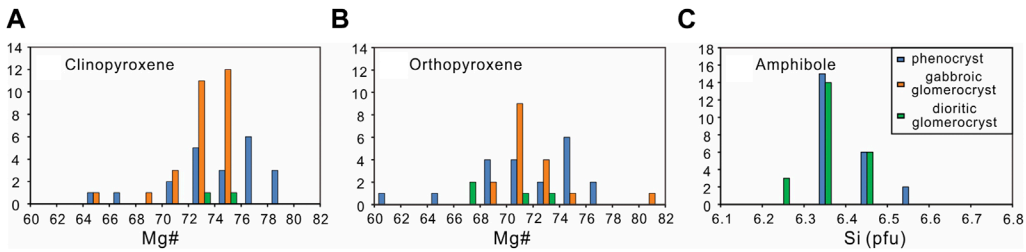

FIGURE 5
Histograms showing the distributions of the core compositions of **(A)** clinopyroxene, **(B)** orthopyroxene, and **(C)** amphibole.

and subhedral plagioclase and orthopyroxene. Clinopyroxene is occasionally absent. Fe-Ti oxides always occur as an interstitial phase. Plagioclases in this type of glomerocryst exhibit high-An, irregular cores surrounded by low-An regions, forming a patchy texture. 2) Assemblages of plagioclase + amphibole ± pyroxene ± Fe-Ti oxides (dioritic glomerocryst) (Figure 3F), ranging in size from 1.7 mm to 5.0 mm, mainly characterized by euhedral and subhedral plagioclase and amphibole as the dominant phases, with pyroxene and Fe-Ti oxides occurring as the subordinate phases. Anhedral pyroxene, euhedral Fe-Ti oxides, and apatite are found as inclusions hosted in some amphiboles. Moreover, a pyroxenite glomerocryst is observed in one sample (DLC-2-2; Figure 3E), in which both orthopyroxene and clinopyroxene crystals are preferentially oriented and arranged in parallel, exhibiting resorption textures.

5.2 Mineral compositions

5.2.1 Plagioclase

Plagioclase phenocryst cores exhibit a broad compositional distribution, with anorthite content ranging from 40 to 59 (Supplementary Table S1). Specifically, plagioclase phenocrysts with cores of relatively higher An (53–59) display oscillatory zoning with variable amplitudes (ΔAn ranging from 3 to 20) or normal zoning. In contrast, those with the cores of An = 40 exhibit patchy zoning and sudden increases in An (ΔAn ranging from 17 to 30) at the cores, followed by oscillatory or normal zoning similar to those with high An cores (53–59). At the rims, the An values of all plagioclases are concentrated between 47 and 57, resembling microcrystals with An = 46–55.

The cores of plagioclases in the gabbroic glomerocryst also exhibit patchy zoning, with high An cores (62) containing low An patches (57), followed by oscillatory zoning with larger amplitudes (ΔAn > 8). There is no oscillatory zoning at the contact between plagioclase and pyroxene, indicating that the oscillatory zoning of plagioclase develops after the formation of the glomerocryst. The plagioclase crystals from the dioritic glomerocryst display oscillatory zoning with varying amplitudes (ΔAn ranging from 2 to 9).

5.2.2 Clinopyroxene

The major element compositions of pyroxenes are listed in both Supplementary Tables S2, S3. Pyroxene formulas were calculated on the basis of four cations and six oxygen ions. Clinopyroxenes in phenocrysts and glomerocrysts are augites, while four phenocrysts are diopsides ($En_{35.78–44.66}$ $Fs_{11.80–21.52}$ $Wo_{40.86–45.90}$; Figure 4A). The Mg# range at the cores of clinopyroxene phenocrysts is 71.67–79.41, with an average of 75.50, mainly concentrated between 72.00 and 78.00 (Supplementary Table S2; Figure 5A). Both normal zoning and reverse zoning are observed at the rims. Two clinopyroxene grains have relatively low Mg# (65.49 and 67.23) and show reverse zoning at the rims (70.06 and 72.04).

Clinopyroxenes in the gabbroic glomerocryst of the Daliuchong dacite exhibit a similar range of Mg# (64.10–76.00) with an average of 73.16, mainly concentrated between 72.00 and 76.00 (Supplementary Table S2; Figure 5A). The Mg# of two grains from the dioritic glomerocryst are 73.24 and 74.70. Additionally, the pyroxenite glomerocryst observed in one sample (DLC-2-2) contains a clinopyroxene with a Mg# of 80.07, which is comparable to the phenocryst with the highest Mg# (79.41).

5.2.3 Orthopyroxene

Orthopyroxene phenocrysts and orthopyroxenes within glomerocrysts are classified as clinoenstatite ($En_{59.15–78.89}$ $Fs_{18.76–39.45}$ $Wo_{1.39–2.98}$), with the exception that two grains from a gabbroic glomerocryst have rims of clinoferrosillite ($En_{46.75–48.19}$ $Fs_{49.17–49.64}$ $Wo_{2.64–3.61}$; Figure 4A). The orthopyroxene phenocrysts have Mg# ranging from 60.65 to 76.68 at the cores, predominantly concentrated between 68.00 and 76.00 (Supplementary Table S3; Figure 5B). Most of these grains exhibit complex compositional variations, including normal zoning (e.g., Mg# ranging from 74.47 to 64.05), reverse zoning (e.g., Mg# ranging from 73.73 to 77.05), and composite zoning [with low Mg# (60.65) at the core, elevated Mg# (74.02) at the mantle, and a sudden drop in Mg# (66.72) at the rim].

Orthopyroxenes from the gabbroic glomerocryst exhibit a similar range of Mg# (68.40–81.09) to that of the phenocrysts, with a compositional peak observed at 70.00–74.00 (Supplementary Table S3; Figure 5B), displaying normal zoning (where Mg# decreases sharply to 49.41–50.40) at the rims. Orthopyroxenes in the dioritic glomerocryst are surrounded by amphibole and plagioclase crystals, with Mg# ranging from 66.65 to 72.81. The Mg# range (73.82–77.10) of orthopyroxenes from the

TABLE 2 Bulk major and trace element compositions and Sr-Nd isotopes of the Daliuchong dacite samples.

Sample	DLC-2-1	DLC-2-2	DLC-2-6	DLC-4-1	DLC-4-3	DLC-4-4
Major element (wt%)						
SiO_2	65.28	65.51	64.20	64.02	64.21	62.99
TiO_2	0.58	0.58	0.58	0.67	0.70	0.72
Al_2O_3	16.09	16.13	16.44	15.96	16.20	16.78
TFe_2O_3	3.56	3.63	3.81	4.20	4.26	4.48
MnO	0.06	0.06	0.06	0.06	0.05	0.07
MgO	0.94	0.87	1.23	1.38	1.36	1.77
CaO	3.37	2.97	3.65	3.37	2.47	3.35
Na_2O	3.45	3.26	3.45	3.49	3.24	3.47
K_2O	3.57	3.61	3.43	3.57	3.73	3.42
P_2O_5	0.13	0.17	0.12	0.16	0.15	0.17
LOI	2.54	2.73	2.56	2.68	3.20	2.46
Total	99.56	99.52	99.52	99.57	99.56	99.69
Trace element (ppm)						
Sc	8.63	8.40	9.10	9.27	8.48	9.37
V	61.2	58.0	63.1	72.5	74.5	77.6
Cr	11.5	11.1	12.6	18.9	16.8	21.3
Co	7.46	6.97	8.53	8.94	8.20	9.57
Ni	4.50	4.46	5.15	12.25	10.75	10.90
Cu	15.1	12.1	11.5	17.2	12.2	10.7
Zn	62.3	59.1	62.9	60.9	59.0	65.5
Ga	19.5	19.0	20.0	18.6	19.3	20.1
Rb	149	150	101	134	121	78.9
Sr	305	289	304	284	208	300
Y	19.7	16.7	28.9	14.8	13.4	19.2
Ti	3447	3483	3489	4040	4178	4292
Zr	140	136	149	117	216	217
Nb	15.2	15.1	15.4	16.3	16.8	17.2
Cs	2.77	3.04	1.17	2.09	2.12	1.25
Ba	605	612	616	628	628	658
La	64.67	70.05	68.50	50.16	43.54	53.96

(Continued on the following page)

TABLE 2 (*Continued*) Bulk major and trace element compositions and Sr-Nd isotopes of the Daliuchong dacite samples.

Sample	DLC-2-1	DLC-2-2	DLC-2-6	DLC-4-1	DLC-4-3	DLC-4-4
Ce	124	124	125	97.1	92.8	107
Pr	14.9	15.5	17.0	11.2	10.2	12.6
Nd	53.3	55.3	64.0	40.4	36.7	46.2
Sm	8.45	8.37	10.31	6.65	6.16	7.46
Eu	1.46	1.44	1.63	1.37	1.23	1.49
Gd	6.86	6.65	8.34	5.42	4.96	6.13
Tb	0.84	0.78	1.06	0.67	0.62	0.78
Dy	4.25	3.87	5.48	3.46	3.23	4.07
Ho	0.77	0.69	1.01	0.61	0.58	0.75
Er	2.22	2.01	2.95	1.77	1.70	2.18
Tm	0.29	0.26	0.40	0.23	0.23	0.29
Yb	1.82	1.67	2.52	1.48	1.48	1.87
Lu	0.26	0.24	0.37	0.21	0.21	0.27
Hf	4.43	4.57	4.69	3.73	5.81	5.75
Ta	1.10	1.15	1.11	1.07	1.10	1.09
Pb	29.5	30.5	29.7	26.3	27.6	29.8
Th	35.1	36.5	35.8	27.4	27.9	28.9
U	3.37	3.50	3.25	2.96	3.25	3.04
Sr-Nd isotopic data						
$^{87}Sr/^{86}Sr$	0.709306	0.709332	0.709294	0.708961	0.708890	0.708956
2σ	0.000006	0.000006	0.000007	0.000007	0.000005	0.000007
$^{143}Nd/^{144}Nd$		0.511988	0.511995	0.512039	0.512023	0.512033
2σ		0.000006	0.000007	0.000006	0.000007	0.000007

pyroxenite glomerocryst is similar to the highest Mg# observed in phenocrysts.

5.2.4 Amphibole

The major element compositions of amphiboles are listed in Supplementary Table S4. Following the amphibole nomenclature proposed by Leake et al. (1997), the amphiboles from the Daliuchong dacite are classified as magnesiohastingsite, pargasite, and edenite (Figures 4B, C). Additionally, the amphibole phenocrysts exhibit a relatively consistent composition range (Si = 6.30–6.56). Glomerocrystic amphiboles display a similar but slightly narrower range for silicon (6.25–6.45; Figure 5C).

5.3 Bulk-rock major and trace element composition

The results of bulk major element and trace element compositions are presented in Table 2. Specifically, the samples from Daliuchong exhibit variable geochemical characteristics, with 64.79–67.69 wt% SiO_2, 0.90–1.82 wt% MgO, 3.67–4.61 wt% $Fe_2O_3^T$, 2.56–3.76 wt% CaO, and 0.59–0.74 wt% TiO_2 contents (normalized to 100%) (Figure 6; Figure 7), even when considering analytical errors. In the total alkalis *vs.* silica (TAS) and K_2O *vs.* SiO_2 diagrams, they fall in the field of dacite and belong to the high-K calc-alkaline series (Figures 6A, B). In the TAS diagram, the Daliuchong dacite [data from this study and Zhang (2017)] does not plot along the evolution line between basalt and andesite;

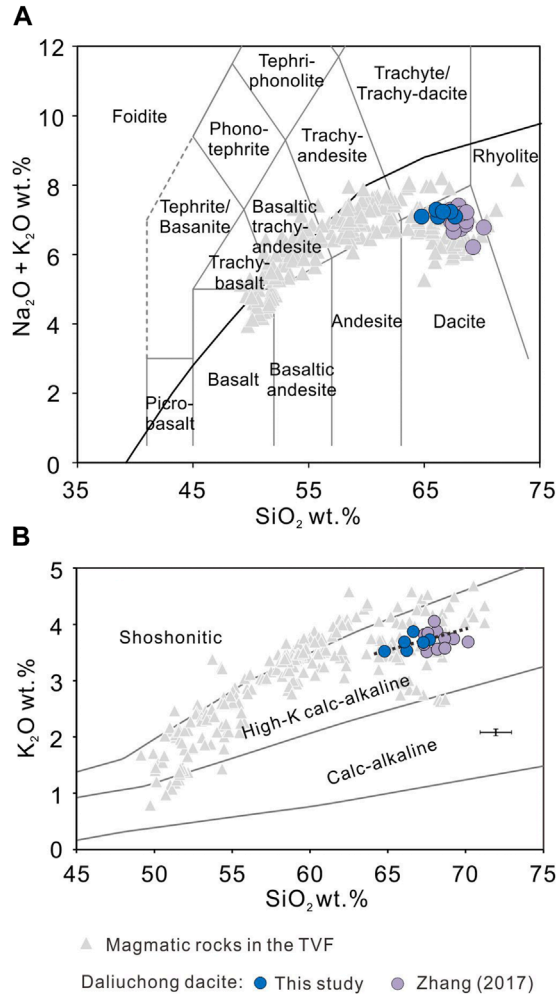

FIGURE 6
(A) Total alkali–silica (TAS) diagram (after Le Bas et al., 1986). **(B)** Diagram of K_2O against SiO_2 (after Peccerillo and Taylor, 1976; Rickwood, 1989). Sources of published data: Fan et al. (1999), Zhao and Fan (2009), Cheng et al. (2012), Li and Zhang (2012), Shi et al. (2012), Yu et al. (2012), Zhang et al. (2012b), Zhou et al. (2012), Zhang et al. (2015), Zou et al. (2014), Cui et al. (2015), Gao et al. (2015), Yao et al. (2016), Li et al. (2017), Zhang (2017), Zou et al. (2017), and Hu et al. (2018). The data represented by the purple circles come from Zhang (2017). The black crossed line in the figure represents the analytical error, which is calculated based on a relative error of less than 3%.

instead, it forms a distinct trend (Figure 6A). Furthermore, in the Harker diagrams, dacite exhibits an approximately linear trend, tending toward mafic magma at the less silicic end member (e.g., Al_2O_3, K_2O, CaO, and MgO) (Figure 7). However, it should be noted that no clear linear trend exists between the most silicic dacitic magma and mafic magma, and the compositional variation is also observed for the more silicic end member. This illustrates that dacite itself exhibits the characteristic of compositional heterogeneity.

All the Daliuchong dacite samples exhibit consistent patterns in the chondrite-normalized diagram, with enriched LREEs contrasting with heavy rare earth elements (HREEs) and displaying a negative Eu anomaly. Additionally, the Tengchong basalt, which has the highest MgO content, exhibits higher REE content than the Daliuchong dacite (Figure 8A). In the primitive mantle-normalized diagram, the Daliuchong samples display moderate enrichments of large-ion lithophile elements (LILEs) such as Rb, Th, U, K, etc., relative depletion of Nb-Ta-Ti, and a positive Pb anomaly (Figure 8B). Furthermore, a negative Sr anomaly is observed among the Daliuchong samples, and the contents of incompatible elements (e.g., Nb, Ta, Zr, and Hf) in the dacite are lower than those in the basalt.

5.4 Bulk-rock Sr-Nd isotopic composition

The bulk Sr and Nd isotope data for the Daliuchong dacite are listed in Table 2. As shown, the Daliuchong dacite exhibits relatively higher initial $^{87}Sr/^{86}Sr$ ratios (0.7089–0.7093) and lower initial $^{143}Nd/^{144}Nd$ ratios (0.51199–0.51203) than mafic rocks in the TVF. Additionally, as depicted in Figure 9, the initial $^{87}Sr/^{86}Sr$ and $^{143}Nd/^{144}Nd$ ratios of the volcanic rocks in the TVF increase and decrease, respectively, with elevated SiO_2 content. Furthermore, Figure 9 also illustrates that the slopes of data for dacite and more mafic rocks are notably different.

6 Discussion

6.1 Estimation of crystallization conditions

6.1.1 Clinopyroxene-liquid thermobarometer

The crystallization conditions of clinopyroxene were estimated using clinopyroxene-liquid thermobarometers developed by Putirka (2008). We selected the bulk composition of the Daliuchong dacite as the potential liquid composition assumed to be in equilibrium with clinopyroxenes. We used the $K_{D(Fe\text{-}Mg)}^{cpx\text{-}liq} = 0.28 \pm 0.08$ to test the equilibrium between clinopyroxene and liquid. The results indicated that the majority of clinopyroxene cores are in equilibrium with the bulk-rock composition of dacite. The crystallization pressure and temperature of clinopyroxene were calculated using equations (30) and (33) from Putirka (2008), yielding P-T conditions for both phenocrystic and glomerocrystic clinopyroxenes of 600–868 MPa and 918°C–972°C, and 564–778 MPa and 915°C–961°C, respectively. Two phenocrystic clinopyroxenes exhibited P-T conditions of 225 MPa and 886°C and 303 MPa and 897°C (Figure 10A; Table 3). Only one clinopyroxene crystal from the gabbroic glomerocryst yielded low P-T conditions, specifically, 457 MPa and 908°C.

6.1.2 Amphibole thermobarometer

The crystallization conditions of amphiboles were estimated using the calcic amphibole-only geothermometer developed by Ridolfi et al. (2023), which is suitable for Mg-rich calcic amphibole in equilibrium with calc-alkaline or alkaline melts. The results of the calculated P-T-fO_2-H_2O_{melt} of amphiboles are presented in Figure 10 and Table 4. The thermobarometer estimation

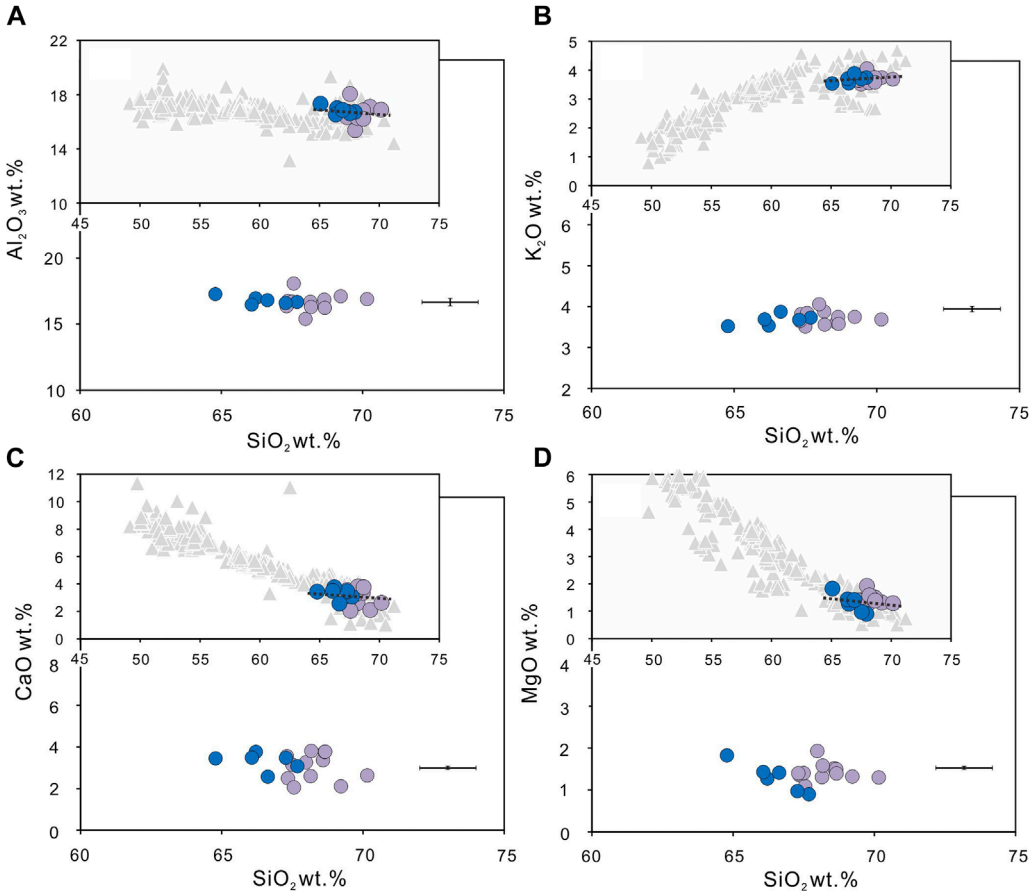

FIGURE 7
Harker diagrams showing the bulk-rock major element compositions of volcanic rocks in the TVF and the Daliuchong dacite. The symbols are the same as in Figure 6. Each diagram includes an error line. The black dotted line represents an approximate trend of the Daliuchong dacite.

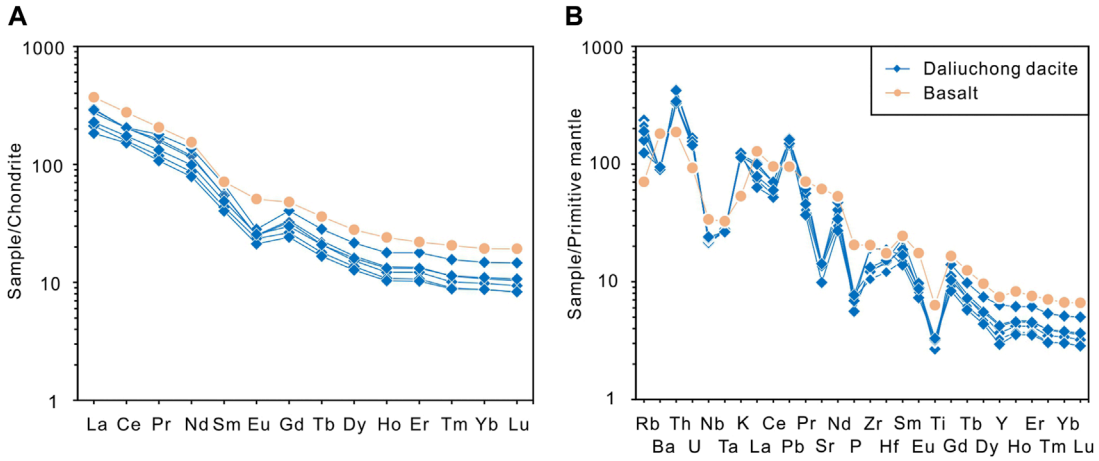

FIGURE 8
(A) Chondrite-normalized rare earth element patterns. **(B)** Primitive mantle-normalized trace element patterns. The data for the Tengchong basalt with the highest MgO are from Cheng et al. (2020).

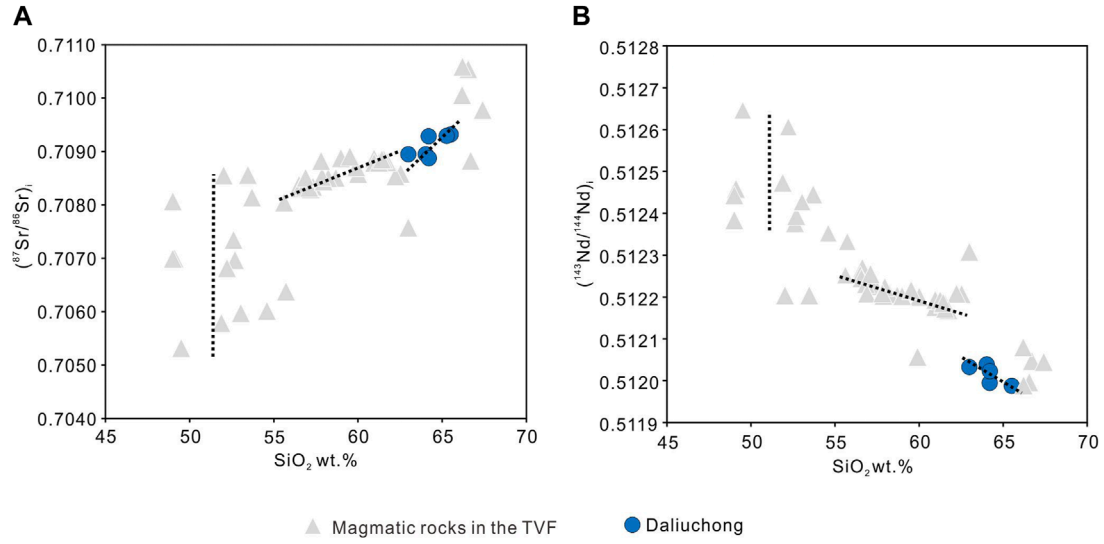

FIGURE 9
$(^{87}Sr/^{86}Sr)_i$ and $(^{143}Nd/^{144}Nd)_i$ *vs.* SiO_2 diagrams. Tengchong volcanic rock data are from Cheng et al. (2020) and Tian et al. (2018). The black dotted lines represent possible evolution trends.

yielded results of 185–258 MPa, 846°C–889°C, ΔNNO = +1.5 to +4.1, 5.0–6.7 wt%, and 200–251 MPa, 824°C–900°C, ΔNNO = +2.0 to +4.4, 4.9–6.6 wt% for phenocryst and glomerocryst, respectively (Figures 10A–C).

Plagioclase and amphibole phenocrysts are the primary phenocryst phases in dacite, exhibiting a range of shapes from euhedral to subhedral. However, clinopyroxene and orthopyroxene phenocrysts are typically anhedral and are only occasionally observed, resulting in a relatively low abundance in our samples. Within the gabbroic glomerocryst, plagioclase generally displays an irregular core, and oscillatory zoning of plagioclase develops after the formation of the glomerocryst. Additionally, the An values of the plagioclase cores in the gabbroic glomerocryst are slightly higher than those of the phenocryst cores. There are two sets of temperature and pressure conditions calculated using clinopyroxene phenocrysts: one set indicates higher pressure and temperature (600–868 MPa, 918°C–972°C) derived from grains with a higher Mg# (71.67–79.41), while two clinopyroxenes with a lower Mg# (65.49 and 67.23) yield lower temperature and pressure conditions (225 and 303 MPa, 886°C and 897°C), similar to those of amphibole phenocrysts and amphiboles in the dioritic glomerocryst (185–258 MPa and 824°C–900°C). The temperature and pressure conditions (564–778 MPa and 915°C–961°C) obtained from clinopyroxenes in the gabbroic glomerocryst are consistent with those obtained from clinopyroxene phenocrysts with high Mg#. Based on these temperature and pressure conditions and mineral textures, we conclude that the pyroxene phenocrysts with high Mg# values and the gabbroic glomerocryst are not products of the fractional crystallization of dacitic magma. Instead, the amphibole and plagioclase phenocrysts and the dioritic glomerocryst crystallized from dacitic magma stored in the shallow magma reservoir in the upper crust.

6.2 Compositional heterogeneity and origin of Daliuchong dacitic magma

The bulk-rock compositions of Daliuchong dacite exhibit diversity, reflected in the variation of approximately 5.4 wt% SiO_2, even when considering analysis errors of up to 2.0 wt%. The dacite samples show an absence of a clear linear trend between the most silicic dacitic magma and mafic magma in the silica variation diagrams (Figure 7). Therefore, the compositional diversity of dacitic magma appears to be an intrinsic property, indicating that the composition of the initially formed dacitic magma is heterogeneous.

We initially explored the possibility that basaltic magmas in the TVF could have generated the dacitic magma. However, the Harker diagrams reveal a divergence between the trend of the Daliuchong dacite and the evolution trend of mafic magma (Figure 7). Similarly, analysis of the TAS diagram indicates that the dacite forms a distinct cluster rather than aligning with the evolution trend of more mafic magma (Figure 6). Furthermore, the comparison of rare earth elements and incompatible element (Nb, Ta, Zr, Hf) contents between the basalt and the Daliuchong dacite (Figure 8) indicates higher levels in the basalt. Additionally, the $^{87}Sr/^{86}Sr$ ratios of the Daliuchong dacite are notably higher than those of basalt, while the $^{143}Nd/^{144}Nd$ ratios are significantly lower (Figure 9), suggesting that the dacitic magma did not result from the fractional crystallization of basaltic magmas. Thus, the formation of the dacitic magma might have involved a completely different process. Based on these observations, we consider that partial melting of the mafic lower crust played a key role in the formation of the dacite.

It is well-known that partial melting of the mafic lower crust is capable of producing dacitic magma (e.g., Beard and Lofgren, 1991; Wolf and Wyllie, 1994; Rapp and Watson, 1995; Winther, 1996; Springer and Seck, 1997). Pyroxenes with high

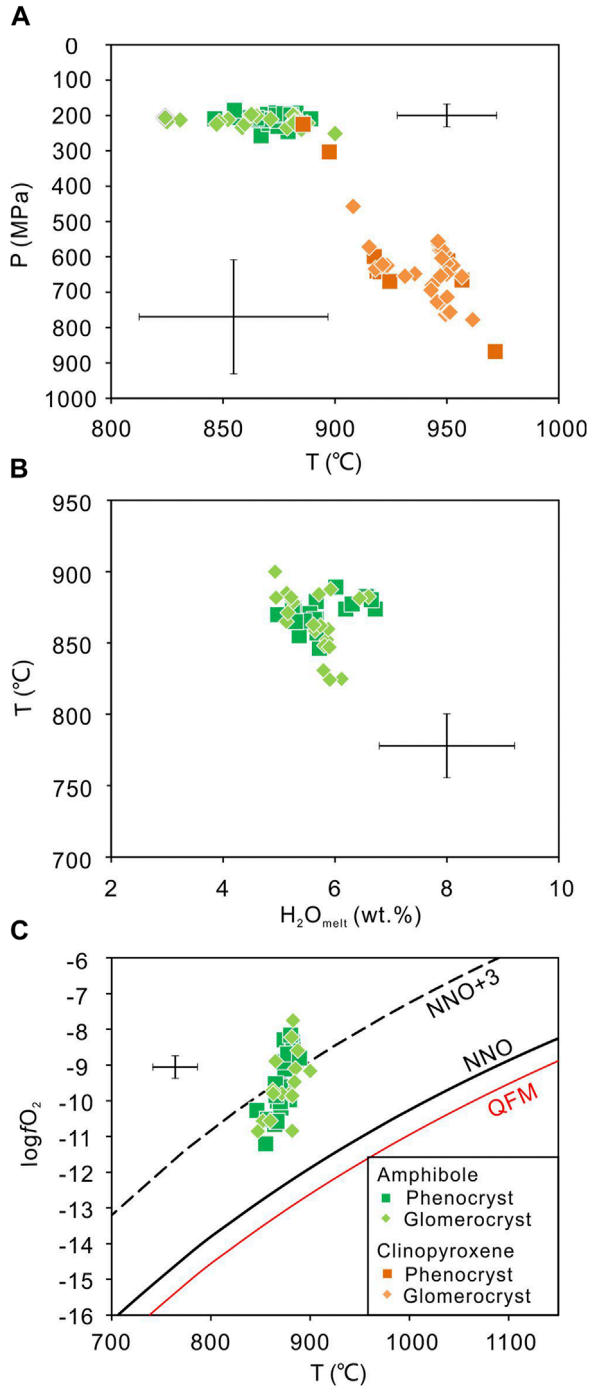

FIGURE 10
(A) Estimated crystallization pressure and temperature of clinopyroxene and amphibole. **(B)** Estimated H_2O content in the melt. **(C)** Estimated oxygen fugacity of melt. The black crossed lines in the figure represent the standard error of the estimate.

Mg# and the gabbroic glomerocryst are not products of the fractional crystallization of dacitic magma. These additions may affect the composition of the primary dacitic magma; however, the amount of high-Mg# pyroxene phenocrysts is rather small; thus, they will not have a significant effect. Therefore, to compare with the experimentally produced dacitic melt, we have only removed the contribution of the gabbroic glomerocryst through mass balance. Specifically, we calculated the mass fraction of the gabbroic glomerocryst using the volume fraction to obtain a more realistic composition of the melt or dacitic magma. The calculation employed the following phase densities: 2.79 g cm^{-3} for plagioclase, 3.2 g cm^{-3} for clinopyroxene, 3.4 g cm^{-3} for orthopyroxene, and 2.6 g cm^{-3} for dacitic magma (excluding the gabbroic glomerocryst) (reference value). Representative compositions of mineral phases were selected based on the compositional peaks in Figure 5. Consequently, the primary composition of the dacitic magma used for comparison was derived by subtracting the composition of the gabbroic glomerocryst from the bulk-rock composition. Comparing the melt composition from previous experiments on the partial melting of mafic crust with the primary bulk-rock composition of the Daliuchong dacite, we observed that the composition of the Daliuchong dacite is similar to that of the experimental melt from Beard and Lofgren (1991) (Figure 11). However, the K_2O content of the Daliuchong dacite is notably higher. The highest K_2O content observed in the experimental melt is 2.61 wt%, which remains lower than the K_2O content found in the Daliuchong dacite (ranging from 3.54 to 4.04 wt%). This could potentially reflect that the lower crust of Tengchong may be compositionally enriched in potassium. We consider that the basic granulite beneath Tengchong could be the source.

Crustal melting can generate heterogeneous dacitic magmas independently. During this process, the Al_2O_3 and FeO^T contents of experimental melts increase as the SiO_2 content decreases, corresponding to increases in temperature and/or water content (Winther, 1996; Tamura and Nakagawa, 2023). Specifically, in the case of crustal melting caused by a single heat source, the presence of a thermal gradient confines the hotter region near the heat source. This results in the formation of a smaller amount of partial melt with high degrees of partial melting in the hotter region. Conversely, the colder region, situated farther away from the heat source, generates a larger body with lower degrees of partial melting (Matsumoto and Nakagawa, 2010). Similar crustal melting processes have been proposed for other magmatic systems, such as the Usu volcano (Matsumoto and Nakagawa, 2010) in Japan and Pinatubo (Tamura and Nakagawa, 2023) in the Philippines. Applying this model to the Daliuchong dacitic magma, we suggest that a higher degree of partial melting near the heat source generates a smaller amount of less silicic melt, while a lower degree of partial melting further from the boundary produces a larger amount of more silicic melt. The widespread distribution of Mg# of pyroxene cores corresponds to the compositional variation of dacitic melts produced by partial melting. Pyroxenes display a series of pronounced or subtle normal and reverse zoning patterns (Figure 12), attributed to the mixing of dacitic melts with varying compositions. The deep magma reservoir indicated by clinopyroxene phenocrysts with high Mg# and glomerocrystic clinopyroxenes mentioned in Section 6.1 may correspond to the location where partial melting produces dacitic melts. Anhedral pyroxene and gabbroic glomerocryst may represent remnants of partial melting within the mafic lower crust. Clinopyroxene phenocrysts with high Mg# and clinopyroxenes in the gabbroic glomerocryst may have re-equilibrated with the melt produced by partial melting, influencing their composition. The pressure range (564–868 MPa) obtained from the clinopyroxene-liquid thermobarometer reflects the pressure condition for the

TABLE 3 Estimated crystallization conditions of clinopyroxene in Daliuchong dacite samples.

		T (°C)	P (MPa)			T (°C)	P (MPa)
	SEE	±42	±160		SEE	±42	±160
Phenocryst	4-3cpx1c	919	640	Gabbroic glomerocryst	4-3cpx9c	923	620
	4-3cpx2c	920	640		4-3cpx10c	915	570
	4-3cpx3c	925	670		4-3cpx11c	921	630
	4-3cpx4c	886	220		4-3cpx12c	931	650
	4-3cpx6c	918	600		4-3cpx13c	918	630
	4-3cpx7c	897	300		4-3cpx14c	908	460
	4-4cpx3c	972	870		4-3cpx15c	921	620
	4-4cpx6c	950	620		4-4cpx9c	953	620
	4-4cpx7c	957	670		4-4cpx10c	950	620
	4-4cpx8c	950	610		4-4cpx11c	957	660
Gabbroic glomerocryst	4-1cpx1c	947	730		4-4cpx12c	949	590
	4-1cpx4c	946	730		4-4cpx13c	961	780
	4-1cpx5c	949	760		4-4cpx14c	950	650
	4-1cpx13c	950	710		4-4cpx15c	946	560
	4-1cpx14c	951	760		4-4cpx16c	947	580
	4-1cpx15c	951	760		4-4cpx17c	947	650
	4-1cpx16c	936	650		4-4cpx18c	948	580
	4-1cpx17c	943	680		4-4cpx19c	948	600
	4-1cpx18c	943	690		4-4cpx20c	946	560

Note. SEE: regression standard error of estimate (σ_{est}) of the model, representing the structural uncertainty.

formation of dacitic melts. Assuming average densities of the upper crust, middle crust, and lower crust in Tengchong are 2.67 g cm^{-3}, 2.80 g cm^{-3}, and 3.10 g cm^{-3}, respectively, the depth (reference value) of the upper crust is estimated to be approximately 0–20 km, the middle crust is 20–27 km, and the lower crust is 27–40 km (Yang et al., 2015). Consequently, the corresponding depth of pressure ranges from 21 to 32 km. Although plagioclase also displays various zoning textures, the oscillatory zoning in the plagioclase crystals exhibits frequent cyclicity with a large amplitude (Figures 13B, C, F). If this is attributed to the mixing of heterogeneous dacitic magmas, a perfect model accounting for the repetitive cycle of crystals in dacitic magmas with different physical and chemical conditions is required, which is obviously unfeasible. Therefore, the oscillatory zoning of plagioclase should be considered independent of this process. The final mixture of heterogeneous melts was stored in the shallow crust at pressures of approximately 185–257 MPa, corresponding to a depth of 7–10 km, forming a hybrid heterogeneous dacitic magma reservoir.

6.3 Magma replenishment and mixing

Mafic magma recharge has been proven to be an effective mechanism for triggering intermediate to acidic volcanic eruptions (Viccaro et al., 2010; Perugini, 2021; Tamura and Nakagawa, 2023). Previously, Gao et al. (2015) suggested that the formation of Early-Middle Pleistocene dacite in the TVF resulted from the mixing of mantle-derived basaltic magma and crustal granite-derived felsic magma, based on bulk-rock geochemistry and isotopic analysis. However, our study proposes that the injection of mafic magma into the Daliuchong dacitic magma resulted in compositional variations within the dacitic magma, ultimately culminating in the eruption of the

TABLE 4 Estimated crystallization conditions of amphibole in Daliuchong dacite samples.

		T (°C)	P (MPa)	logfO_2 (ΔNNO)	H_2O_{melt} (wt%)
	SEE	±23	±12%	±0.3	±14%
Phenocryst	2-1Hb1c	867	210	2.5	5.5
	2-1Hb3c	846	210	2.6	5.7
	2-2Hb1c	857	210	2.2	5.7
	2-3Hb1c	879	250	2.3	5.7
	2-5Hb1c	855	180	1.5	5.4
	2-5Hb2c	867	260	-	5.7
	4-1Hb1c	871	220	2.2	5.6
	4-1Hb2c	874	230	2.6	5.3
	4-1Hb4c	874	190	4.1	6.7
	4-2Hb1c	882	200	3.8	6.6
	4-2Hb2c	883	190	3.6	6.6
	4-2Hb3c	874	200	3.4	6.2
	4-3Hb1c	870	200	2.4	5.2
	4-3Hb2c	867	210	1.9	5.6
	4-3Hb2r	864	210	1.9	5.8
	4-3Hb3c	865	210	2.7	5.4
	4-3Hb4c	877	200	3.6	6.3
	4-3Hb5c	889	210	3.3	6.0
	4-3Hb6c	880	200	4.1	6.6
	4-4Hb1c	870	210	2.8	5.0
	4-4Hb2c	874	210	3.2	5.2
	4-4Hb3c	865	210	3.0	5.3
Dioritic glomerocryst	2-2Hb2c1	831	210	-	5.8
	2-2Hb2c2	825	220	-	6.1
	2-2Hb3c	824	210	-	5.9
	2-2Hb4c	859	230	-	5.6
	2-4Hb1c	852	210	2.2	5.9
	2-4Hb2c	860	220	2.1	5.9
	2-6Hb1c	848	220	-	5.8
	2-6Hb2c	847	220	2.0	5.9
	4-1Hb4c	874	190	4.1	6.7
	4-4Hb4c	865	200	3.6	5.1
	4-4Hb5c	879	230	2.4	5.3
	4-4Hb6c	885	240	-	5.1
	4-4Hb7c	871	210	2.6	5.2
	4-4Hb8c	885	240	3.0	5.1
	4-4Hb8r	876	220	2.5	5.4
Dioritic glomerocryst	SEE	±23	±12%	±0.3	±14%
	4-4Hb9c	900	250	2.7	4.9
	4-4Hb10c	883	200	4.4	6.6
	4-4Hb11c	881	200	4.0	6.4
	4-4Hb12c	888	220	3.5	5.9
	4-4Hb13c	884	220	2.7	5.7
	4-4Hb14c	862	200	2.9	5.7
	4-4Hb15c	882	220	2.3	5.2
	4-4Hb16c	863	200	2.8	5.6
	4-4Hb17c	882	220	1.4	4.9

Note. SEE: regression standard error of estimate (σ_{est}) of the model, representing the structural uncertainty. NNO, Ni-NiO buffer.

Daliuchong volcano. The mixing between mafic and dacitic magmas played a pivotal role in the formation and eruption of the Daliuchong dacite, as supported by our new observations of crystal texture, composition, and bulk-rock characteristics of the Daliuchong dacite.

Plagioclase crystals from the Daliuchong dacite exhibit a variety of textures that can be categorized into two groups: 1) Growth textures, such as coarse-sieve texture, fine-sieve texture, oscillatory zoning, and patchy texture with an eroded core, which are attributed to changes in magma temperature, pressure, or composition; and 2) Morphological textures, including glomerocryst, synneusis, microlite, and swallow-tailed crystal, which result from dynamic magma processes such as convection, degassing, and explosive eruption (Renjith, 2014).

The formation of sieve textures in plagioclase can be attributed to two main processes: reaction with a hotter Ca-rich melt (Tsuchiyama, 1985) and rapid decompression (Nelson and Montana, 1992). It is worth noting that these processes typically result in

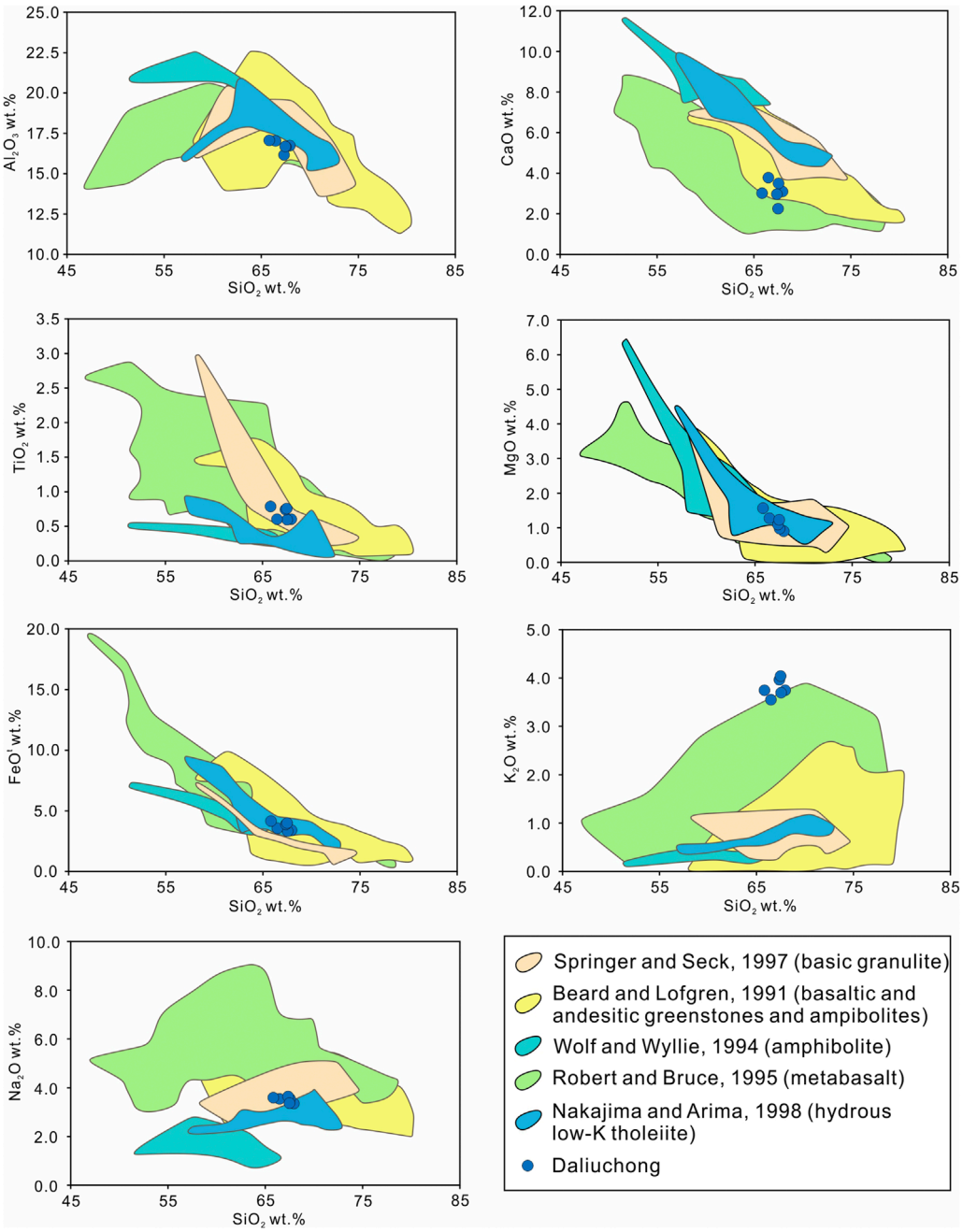

FIGURE 11
Comparison between the compositions of experimental melts obtained in representative dehydration melting studies of metabasalts performed at middle to lower crustal pressures (Beard and Lofgren, 1991; Wolf and Wyllie, 1994; Rapp and Watson, 1995; Winther, 1996; Springer and Seck, 1997; Nakajima and Arima, 1998) and the original composition of the Daliuchong dacite, which was calculated by mass balance (see Section 6.2 of text for details).

different sizes of sieves. Reaction with a hotter calcic melt leads to partial dissolution, starting from the surface of the plagioclase and progressing inward, resulting in a fine-sieve texture. In contrast, rapid decompression at a constant temperature will produce a coarse-sieve texture (Blundy and Cashman, 2001; 2005; Renjith, 2014). At high pressures, equilibrium plagioclase tends to exhibit more sodic composition than at lower pressures (Panjasawatwong et al., 1995; Ustunisik et al., 2014; Bennett et al., 2019). Decompression from high pressure to low pressure under H_2O-undersaturated conditions will lead to resorption and subsequent crystallization of plagioclase with higher An content and constant Ti content (Nelson and Montana, 1992; Bennett et al., 2019). Conversely, decompression under H_2O-saturated conditions can result in degassing and crystallization of more sodic plagioclase (Blundy and Cashman, 2005; Bennett et al., 2019). The size and density (number of sieves per unit area) of coarse sieves increase

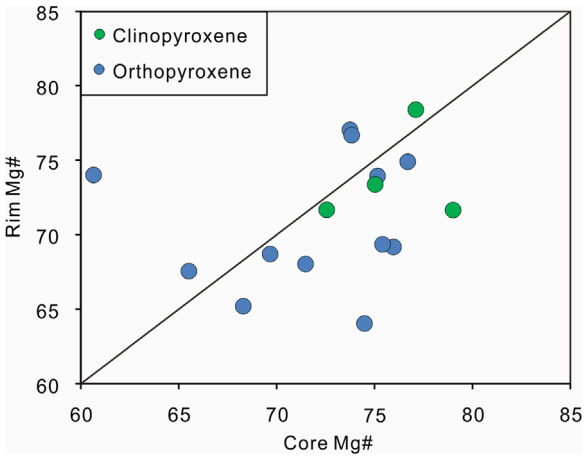

FIGURE 12
Core-rim zoning diagram of pyroxene of the Daliuchong dacite.

outward, suggesting that the rate of dissolution varies, resulting from variations in the rate of decompression under H_2O-undersaturated conditions or the H_2O content dissolved in the magma (Viccaro et al., 2010).

The patchy zoning of the plagioclases found in the gabbroic glomerocryst exhibits the characteristic of a high An irregular core surrounded by low An regions (Figure 13F), consistent with crystallization caused by decompression under water-saturated conditions. The first type of plagioclase displays coarse-sieve textures in the cores and is characterized by the low An core surrounded by high An regions (Figures 13A, B), which contrasts with the patchy zoning of plagioclases in the gabbroic glomerocryst. This type of plagioclase is consistent with the resorption and regrowth driven by decompression under H_2O-undersaturated conditions and may represent xenocrysts entrained by ascending mafic magmas. The density and size of the sieves may be related to the decompression rate. The fine-sieve textures appearing at the margin of the *type 3* plagioclase, as well as the subsequent overgrown rim with higher An (Figure 13D), indicate that the dacitic magma was recharged by hotter, Ca-rich mafic magma(s).

Oscillatory zoning is observed in relatively small grains and the margins of large grains with a coarse-sieve core. Oscillatory zoning can develop through two processes: 1) The growth of crystals in melts where temperature, $P(H_2O)$, and/or composition vary regularly (Singer et al., 1995); 2) the dynamics of crystal growth rate (Pearce, 1994).

Most oscillatory zoning patterns of plagioclase crystals from the Daliuchong samples are commonly associated with minor resorption. Changes in pressure, temperature, water content, and bulk composition due to convection within different zones or the recharge of new magmas may be the primary causes of oscillatory zoning formation. The significant variation in An content ($\Delta An > 5$) and concurrent variation in FeO content observed in the oscillatory zoning (Figures 13B, C) suggest substantial changes in the magmatic environment [$P(H_2O)$, T, melt composition]. However, partial amplitudes of the oscillatory zoning can reach $\Delta An = 15–20$, indicating crystallization of this oscillatory zoning associated with a more mafic magma, revealing the replenishment of mafic magma in the dacitic magma. Some amphibole phenocrysts exhibit embayed textures. Additionally, in the Harker diagrams, we observe that the dacite tends to approach mafic magma at the less silicic end member, indicating compositional alteration of the dacitic magma related to the injection of mafic magma. Moreover, there is evidence of multiple reverse zoning with significant ΔAn in the oscillatory zoning region, suggesting several occurrences of intermittent mafic magma replenishment events. Noticeable reverse zoning is observed at the rims of certain plagioclase phenocrysts, indicating that the last recharge of mafic magma likely triggered the explosive eruption of the Daliuchong dacitic magma.

6.4 Model of the magma plumbing system of the Daliuchong volcano

This study aims to explore the magma plumbing system of the Daliuchong dacitic volcano. As stated above, we here propose the following pre-eruptive processes for the Daliuchong dacite (Figure 14): 1) Mantle-derived mafic magma intruded and stagnated beneath Daliuchong, resulting in partial melting of the heterogeneous mafic lower crust; 2) crustal melting occurred at a depth of 21–32 km. As a result of the thermal gradient induced by varying distances from the heat source (the mafic magma reservoir), the lower crust underwent different degrees of partial melting, creating a mush zone where melts coexist with residual crystals. Subsequently, these melts accumulated into numerous relatively small and isolated sill-shaped magma pockets with varying compositions. Consequently, areas farther from the heat source produced a large number of partially melted bodies with lower degrees of partial melting, whereas areas closer to the heat source generated fewer partially melted bodies with higher degrees of partial melting; 3) these molten bodies grew and eventually mixed with each other, the mixed magma ascended and was stored in the shallow crust (at a depth of 7–10 km). This mixed magma then underwent crystallization of plagioclase, amphibole, Fe-Ti oxides, and small amounts of pyroxene and apatite. 4) Intermittent injection of mafic magma into the shallow crust, where the dacitic magma was stored, resulted in the formation of disequilibrium textures in phenocrysts and compositional variations in the dacitic magma. 5) The final injection of mafic magma induced high pressure and triggered the explosive eruption of the Daliuchong dacitic magma. During this eruption, the construction of the Daliuchong volcanic cone was completed. In the later stage of the eruption, as energy waned, the eruption transitioned gradually to effusive. Eventually, the last minor amount of magma was extruded and emplaced in the conduit, concluding the volcanic activity.

7 Conclusion

We have investigated the formation and pre-eruptive evolution processes of the Daliuchong dacite by analyzing the bulk-rock major and trace elements, Sr-Nd isotopes, and mineral

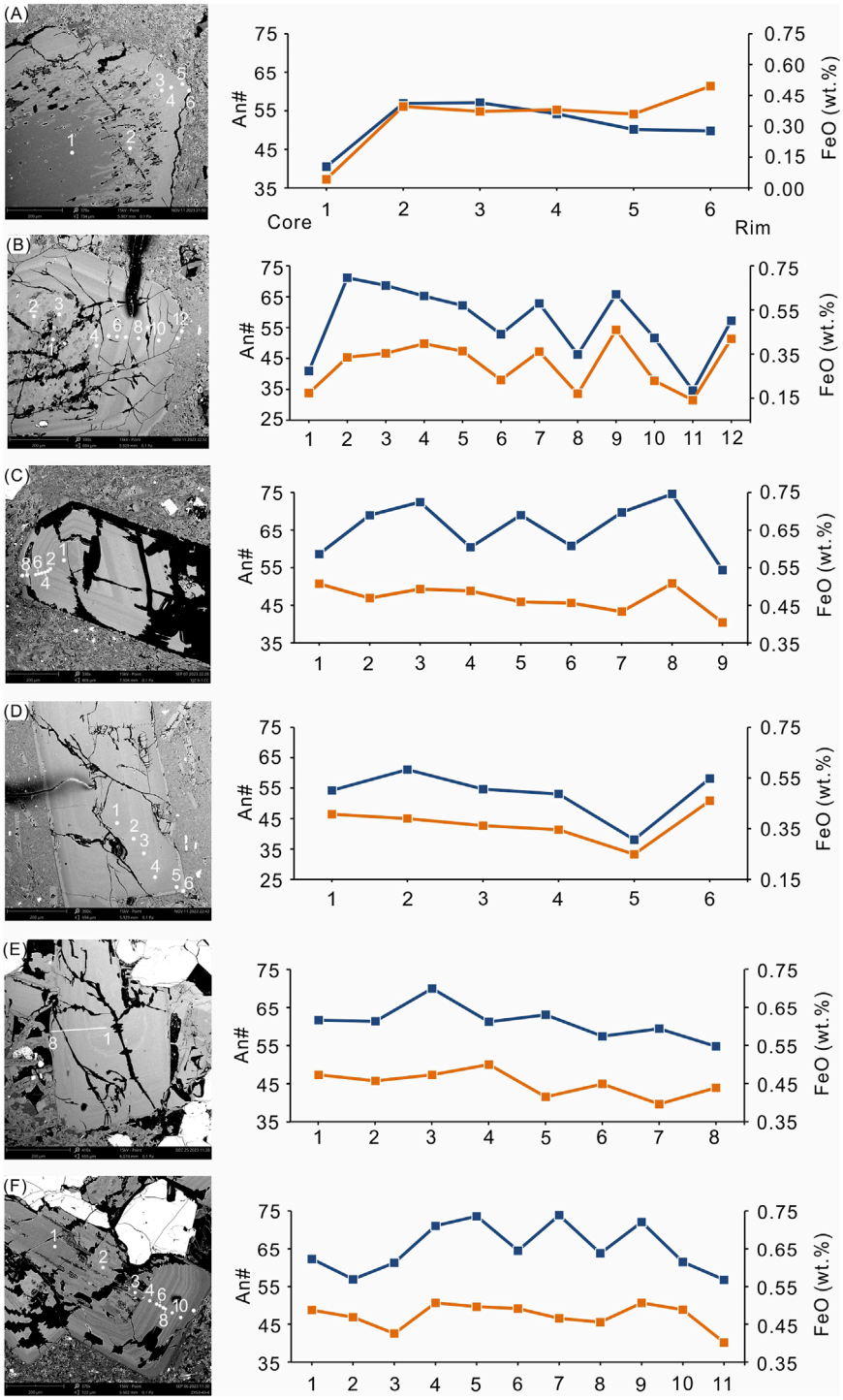

FIGURE 13
Zoning profiles of plagioclase phenocrysts. **(A-B)** *Type 1* plagioclase. **(C)** *Type 2* plagioclase. **(D)** *Type 3* plagioclase. **(E)** Plagioclase in the dioritic glomerocryst. **(F)** Plagioclase in the gabbroic glomerocryst.

textures and chemistry of the Daliuchong dacite and comparing the melt compositions of previous mafic lower crustal melting experiments with its composition. The important findings are as follows.

(1) The Daliuchong dacite exhibits compositional heterogeneity, arising not only from the injection of mafic magma but also from inherent heterogeneity within the dacite itself.

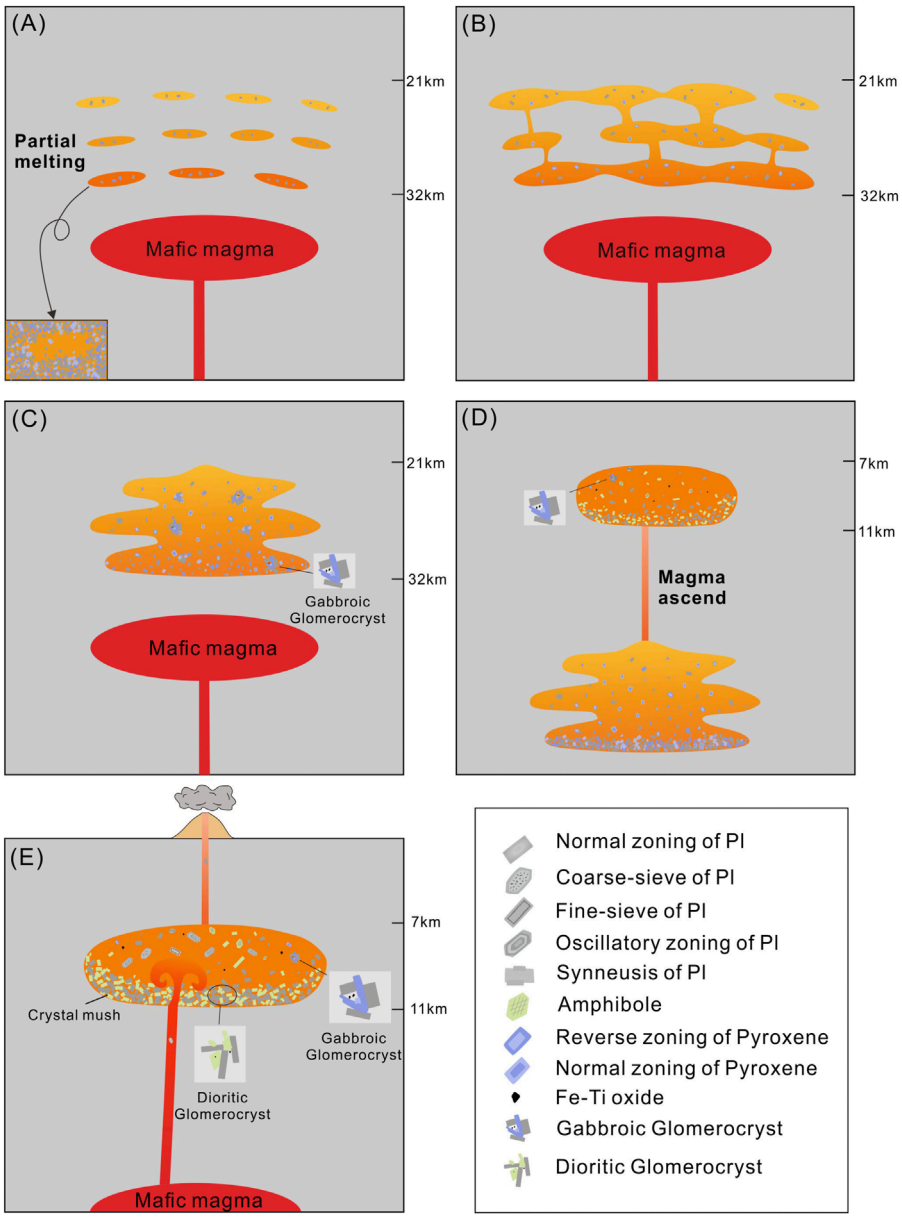

FIGURE 14
Magma plumbing system beneath Daliuchong. **(A)** Mafic magma intrusion and partial melting of the mafic lower crust resulted in the formation of a mush zone where the melts coexist with residual crystals. Subsequently, these melts accumulated to form small and separated sill-shaped magma pockets with varying compositions as a result of a thermal gradient. **(B)** Small magma pockets grew and connected. **(C)** A large heterogeneous dacitic reservoir was formed at a depth of 21–32 km. **(D)** Dacitic magma ascended and was stored in the shallow crust (7–10 km), where it underwent crystallization of plagioclase, amphibole, Fe-Ti oxides, and small amounts of pyroxene and apatite. **(E)** The injection of mafic magma caused magma overpressure, triggering the explosive eruption of the dacitic magma. See text for details.

(2) The Daliuchong dacite cannot be produced through fractional crystallization of basaltic magma. The comparison of the melt compositions generated from the melting experiments of the mafic lower crust with the composition of the Daliuchong dacite supports the formation of the Daliuchong dacite by the partial melting of the mafic lower crust. The partial melting with varying degrees of the mafic lower crust due to a thermal gradient resulted in the compositional heterogeneity of the initially dacitic magma.

(3) Clinopyroxene and amphibole record two distinct magma reservoirs beneath Daliuchong, with the deep magma reservoir (21–32 km) serving as the reservoir for molten crustal melts, containing residual pyroxene crystals and gabbroic glomerocryst. Subsequently, the magma ascended and settled at a shallow depth (7–10 km), undergoing crystallization of plagioclase, amphibole, Fe-Ti oxides, and small amounts of pyroxene and apatite. The environment of the shallow magma reservoir, as recorded by amphibole, is enriched with water (4.9–6.7 wt%) and oxidized (ΔNNO = +1.5 to +4.4).

(4) The mafic magma was intermittently injected into the shallow magma reservoir. The final injection of mafic magma triggered the eruption of the Daliuchong volcano. This suggests that the role of mafic primitive magma replenishment in the formation and evolution of dacites cannot be neglected. The development of highly evolved, dacitic magmas in comparable tectonic environments may be linked to the mechanisms uncovered in our investigation of Daliuchong.

Data availability statement

The original contributions presented in the study are included in the article/Supplementary Material; further inquiries can be directed to the corresponding authors.

Author contributions

CS: data curation, investigation, methodology, visualization, and writing–original draft. MW: funding acquisition, methodology, and writing–review and editing. DL: data curation, methodology, visualization, and writing–review and editing. TH: funding acquisition, methodology, and writing–review and editing.

Funding

The author(s) declare financial support was received for the research, authorship, and/or publication of this article. This research has been supported by the National Natural Science Foundation of China (Nos: 42372058 and 42102048). MW is supported by the Open Project Program of Hebei Province Collaborative Innovation Center for Strategic Critical Mineral Research, Hebei GEO University, China (HGUXT-2023-1). The authors also acknowledge support by the "Deep-time Digital Earth" Science and Technology Leading Talents Team Funds for the Central Universities for the Frontiers Science Center for Deep-time Digital Earth, China University of Geosciences (Beijing) (Fundamental Research Funds for the Central Universities; grant number: 2652023001).

Acknowledgments

The authors thank Weiya Yu and Shiquan Huang for their help in the field investigation. Detailed reviews by Editor Valerio Acocella, Nick Varley, and two reviewers have significantly improved the manuscript.

Conflict of interest

The authors declare that the research was conducted in the absence of any commercial or financial relationships that could be construed as a potential conflict of interest.

Publisher's note

Supplementary material

The Supplementary Material for this article can be found online at: https://www.frontiersin.org/articles/10.3389/feart.2024.1376492/full#supplementary-material

References

Arce, J. L., Macias, J. L., Gardner, J. E., and Layer, P. W. (2006). A 2.5 ka History of Dacitic Magmatism at Nevado de Toluca, Mexico: Petrological, $^{40}Ar/^{39}Ar$ Dating, and Experimental Constraints on Petrogenesis. *J. Petrol.* 47 (3), 457–479. doi:10.1093/petrology/egi082

Banaszak, M. (2014). *Differentiation regimes in the Central Andean magma systems: case studies of Taapaca and Parinacota volcanoes, Northern Chile*. Göttingen, Lower Saxony , Germany: Georg-August University School of Science GAUSS.

Beard, J. S., and Lofgren, G. E. (1991). Dehydration melting and water-saturated melting of basaltic and andesitic greenstones and amphibolites at 1, 3, and 6.9 kb. *J. Petrol.* 32 (2), 365–401. doi:10.1093/petrology/32.2.365

Bennett, E. N., Lissenberg, C. J., and Cashman, K. V. (2019). The significance of plagioclase textures in mid-ocean ridge basalt (Gakkel Ridge, Arctic Ocean). *Contrib. Mineral. Petr.* 174 (49), 1–22. doi:10.1007/s00410-019-1587-1

Blundy, J., and Cashman, K. (2001). Ascent-driven crystallisation of dacite magmas at mount St helens, 1980–1986. *Contrib. Mineral. Petr.* 140 (6), 631–650. doi:10.1007/s004100000219

Blundy, J., and Cashman, K. (2005). Rapid decompression-driven crystallization recorded by melt inclusions from Mount St. Helens Volcano. *Geology* 33 (10), 793–796. doi:10.1130/G21668.1

Browne, B., Izbekov, P., Eichelberger, J., and Churikova, T. (2013). Pre-eruptive storage conditions of the Holocene dacite erupted from kizimen volcano, kamchatka. *Int. Geo. Rev.* 52 (1), 95–110. doi:10.1080/00206810903332413

Cadoux, A., Scaillet, B., Druitt, T. H., and Deloule, E. (2014). Magma storage conditions of large plinian eruptions of Santorini volcano (Greece). *J. Petrol.* 55 (6), 1129–1171. doi:10.1093/petrology/egu021

Cassidy, M., Manga, M., Cashman, K., and Bachmann, O. (2018). Controls on explosive-effusive volcanic eruption styles. *Nat. Commun.* 9 (2839), 1–16. doi:10.1038/s41467-018-05293-3

Cheng, Z. H., Guo, Z. F., Dingwell, D. B., Li, X. H., Zhang, M. L., Liu, J. Q., et al. (2020). Geochemistry and petrogenesis of the post-collisional high-K calc-alkaline magmatic rocks in Tengchong, SE Tibet. *J. Asian Earth Sci.* 193, 104309. doi:10.1016/j.jseaes.2020.104309

Cottrell, E., Gardner, J. E., and Rutherford, M. J. (1999). Petrologic and experimental evidence for the movement and heating of the pre-eruptive Minoan rhyodacite (Santorini, Greece). *Contrib. Mineral. Petr.* 135 (4), 315–331. doi:10.1007/s004100050514

Degruyter, W., Huber, C., Bachmann, O., Cooper, K. M., and Kent, A. J. R. (2017). Influence of exsolved volatiles on reheating silicic magmas by recharge and consequences for eruptive style at volcán quizapu (Chile). *Geochem. Geophy. Geosy.* 18 (11), 4123–4135. doi:10.1002/2017GC007219

Espinosa, V. D., Arce, J. L., and Castro-Govea, R. (2021). Pre-eruptive conditions and reheating of dacitic magma (Malinche Pumice II Plinian eruption) at La Malinche volcano, Central Mexico. *J. Volcanol. Geotherm. Res.* 419, 107368. doi:10.1016/j.jvolgeores.2021.107368

First, E. C., Hammer, J. E., Ruprecht, P., and Rutherford, M. (2021). Experimental constraints on dacite magma storage beneath Volcán Quizapu, Chile. *J. Petrol.* 62 (5), 549–559. doi:10.1093/petrology/egab027

Gao, J. F., Zhou, M. F., Robinson, P. T., Wang, C. Y., Zhao, J. H., and Malpas, J. (2015). Magma mixing recorded by Sr isotopes of plagioclase from dacites of the Quaternary Tengchong volcanic field, SE Tibetan Plateau. *J. Asian Earth Sci.* 98, 1–17. doi:10.1016/j.jseaes.2014.10.036

Grove, T. L., Baker, M. B., Price, R. C., Parman, S. W., Elkins-Tanton, L. T., Chatterjee, N., et al. (2005). Magnesian andesite and dacite lavas from Mt. Shasta, northern California: products of fractional crystallization of H_2O-rich mantle melts. *Contrib. Mineral. Petr.* 148 (5), 542–565. doi:10.1007/s00410-004-0619-6

Haase, K. M., Stroncik, N., Garbe-Schönberg, D., and Stoffers, P. (2006). Formation of island arc dacite magmas by extreme crystal fractionation: an example from Brothers Seamount, Kermadec island arc (SW Pacific). *J. Volcanol. Geotherm. Res.* 152 (3-4), 316–330. doi:10.1016/j.jvolgeores.2005.10.010

Holtz, F., Sato, H., Lewis, J., Behrens, H., and Nakada, S. (2005). Experimental petrology of the 1991-1995 unzen dacite, Japan. Part I: phase relations, phase composition and pre-eruptive conditions. *J. Petrol.* 46 (2), 319–337. doi:10.1093/petrology/egh077

Huang, X. W., Zhou, M. F., Wang, C. Y., Robinson, P. T., Zhao, J., and Qi, L. (2013). Chalcophile element constraints on magma differentiation of Quaternary volcanoes in Tengchong, SW China. *J. Asian Earth Sci.* 76, 1–11. doi:10.1016/j.jseaes.2013.07.020

Jiang, C. S., Zhou, R. Q., and Yao, X. Z. (1998). Fault structure of Tengchong volcano. *J. Seismol. Res.* 21 (4), 40–46. (in Chinese with English abstract).

Jiang, C. S., Zhou, R. Q., and Zhao, C. P. (2003). The relationship between the tectonic geomorphic features and volcano activity in Tengchong region. *J. Seismol. Res.* 26 (4), 361–366. (in Chinese with English abstract).

Johnson, M. C., and Rutherford, M. J. (1989). Experimentally determined conditions in the Fish Canyon Tuff, Colorado, magma chamber. *J. Petrol.* 30 (3), 711–737. doi:10.1093/petrology/30.3.711

Knafelc, J., Bryan, S. E., Gust, D., and Cathey, H. E. (2020). Defining pre-eruptive conditions of the havre 2012 submarine rhyolite eruption using crystal archives. *Front. Earth Sci.* 8, 310. doi:10.3389/feart.2020.00310

Leake, B. E., Woolley, A. R., Arps, C. E. S., Birch, W. D., Gilbert, M. C., Grice, J. D., et al. (1997). Nomenclature of amphiboles: report of the subcommittee on amphiboles of the international mineralogical association, commission on new minerals and mineral names. *Am. Mineral.* 82 (9-10), 1019–1037.

Le Bas, M. J., Le Maitre, R. W., Streckeisen, A., and Zanettin, E. (1986). A chemical classification of volcanic rocks based on the total alkali-silica diagram. *J. Petrol.* 27 (3), 745–750. doi:10.1093/petrology/27.3.745

Li, N., Wei, H. Q., Zhang, L. Y., Zhao, Y. W., Zhao, B., Zhao, Z. Q., et al. (2014a). Discovery of Daliuchong volcanic edifice in Tengchong, yunnan province and its significance. *Acta Petrol* 30 (12), 3627–3634. (in Chinese with English abstract).

Li, N., and Zhang, L. Y. (2011). A study on volcanic minerals and hosted melt inclusions in newly-erupted Tengchong volcanic rocks, Yunnan province. *Acta Petrol* 27 (10), 2842–2854. (in Chinese with English abstract).

Li, N., Zhao, Y. W., Zhang, L. Y., and Wang, J. L. (2020). The quaternary eruptive sequence of the Tengchong volcanic group, southwestern China. *Lithos* 354-355, 105173. doi:10.1016/j.lithos.2019.105173

Li, X., Liu, J. Q., Sun, C. Q., Du, D. D., and Wang, S. (2014b). The magma source properties and evolution of Holocene volcanoes in Tengchong, Yunnan Province, SW China. *Seismol. Geol.* 36 (4), 991–1008. (in Chinese with English abstract). doi:10.3969/j.issn.0253-4967.2014.04.005

Matsumoto, A., and Nakagawa, M. (2010). Formation and evolution of silicic magma plumbing system: petrology of the volcanic rocks of Usu volcano, Hokkaido, Japan. *J. Volcanol. Geotherm. Res.* 196 (3-4), 185–207. doi:10.1016/j.jvolgeores.2010.07.014

Millet, M., Tutt, C. M., Handler, M. R., and Baker, J. A. (2014). Processes and time scales of dacite magma assembly and eruption at Tauhara volcano, Taupo Volcanic Zone, New Zealand. *Geochem. Geophy. Geosy.* 15 (1), 213–237. doi:10.1002/2013GC005016

Nakajima, K., and Arima, M. (1998). Melting experiments on hydrous low-K tholeiite: implications for the genesis of tonalitic crust in the Izu–Bonin–Mariana arc. *Isl. Arc* 7 (3), 359–373. doi:10.1111/j.1440-1738.1998.00195.x

Nelson, S. T., and Montana, A. (1992). Sieve-textured plagioclase in volcanic rocks produced by rapid decompression. *Am. Mineral.* 77 (11-12), 1242–1249.

Panjasawatwong, Y., Danyushevsky, L. V., Crawford, A. J., and Harris, K. L. (1995). An experimental study of the effects of melt composition on plagioclase; melt equilibria at 5 and 10 kbar; implications for the origin of magmatic high-An plagioclase. *Contrib. Mineral. Petr.* 118 (4), 420–432. doi:10.1007/s004100050024

Pearce, T. H. (1994). "Recent work on osillatory zoning in plagioclase," in *Feldspars and their reactions. Nato asi series, series C: mathematical and physical Sciences 421*. Editor Parsons (London, UK: Kluwer Acad. Pub), 313–349. doi:10.1007/978-94-011-1106-5_8

Peccerillo, A., and Taylor, S. R. (1976). Geochemistry of Eocene calc-alkaline volcanic rocks from the Kastamonu area, northern Turkey. *Contrib. Mineral. Petr.* 58 (1), 63–81. doi:10.1007/BF00384745

Perugini, D. (2021). Magma mixing: the trigger for explosive volcanic eruptions. *Adv. Volcanol.*, 135–148. doi:10.1007/978-3-030-81811-1_10

Prouteau, G., and Scaillet, B. (2003). Experimental constraints on the origin of the 1991 Pinatubo dacite. *J. Petrol.* 44 (12), 2203–2241. doi:10.1093/petrology/egg075

Putirka, K. D. (2008). Thermometers and barometers for volcanic systems. *Rev. Mineral. Geochem.* 69 (1), 61–120. doi:10.2138/rmg.2008.69.3

Rapp, R. P., and Watson, E. B. (1995). Dehydration melting of metabasalt at 8-32 kbar; implications for continental growth and crust-mantle recycling. *J. Petrol.* 36 (4), 891–931. doi:10.1093/petrology/36.4.891

Renjith, M. L. (2014). Micro-textures in plagioclase from 1994–1995 eruption, Barren Island Volcano: evidence of dynamic magma plumbing system in the Andaman subduction zone. *Geosci. Front.* 5 (1), 113–126. doi:10.1016/j.gsf.2013.03.006

Rickwood, P. C. (1989). Boundary lines within petrologic diagrams which use oxides of major and minor elements. *Lithos* 22 (4), 247–263. doi:10.1016/0024-4937(89)90028-5

Ridolfi, F., Almeev, R. R., Ozerov, A. Y., and Holtz, F. (2023). Amp-TB2 protocol and its application to amphiboles from recent, historical and pre-historical eruptions of the bezymianny volcano, kamchatka. *Minerals-Basel.* 13 (11), 1394. doi:10.3390/min13111394

Rutherford, M. J., and Devine, J. D. (1988). The may 18, 1980, eruption of mount St. Helens 3. Stability and chemistry of amphibole in the magma chamber. *J. Geophys. Res.* 93 (B10), 11949–11959. doi:10.1029/JB093iB10p11949

Scaillet, B., and Evans, B. W. (1999). The 15 june 1991 eruption of mount Pinatubo. I. Phase equilibria and pre-eruption P - T - fO_2 - fH_2O conditions of the dacite magma. *J. Petrol.* 40 (3), 381–411. doi:10.1093/petroj/40.3.381

Sigurdsson, H., Carey, S., and Davis, A. (1985). The may 18, 1980, eruption of mount St. Helens 1. Melt composition and experimental phase equilibria. *J. Geophys. Res.* 90 (B4), 2929–2947. doi:10.1029/JB090iB04p02929

Singer, B. S., Dungan, M. A., and Layne, G. D. (1995). Textures and Sr, Ba, Mg, Fe, K, and Ti compositional profiles in volcanic plagioclase: clues to the dynamics of calc-alkaline magma chambers. *Am. Mineral.* 80 (7-8), 776–798. doi:10.2138/am-1995-7-815

Springer, W., and Seck, H. A. (1997). Partial fusion of basic granulites at 5 to 15 kbar; implications for the origin of TTG magmas. *Contrib. Mineral. Petr.* 127 (1), 30–45. doi:10.1007/s004100050263

Tamura, T., and Nakagawa, M. (2023). New petrological and geochemical insights into the magma plumbing system of the 1991 Pinatubo eruption. *Contrib. Mineral. Petr.* 178 (43), 1–25. doi:10.1007/s00410-023-02022-y

Tapponnier, P., Lacassin, R., Leloup, P. H., Schärer, U., Zhong, D. L., Wu, H. W., et al. (1990). The ailao Shan/red river metamorphic belt: tertiary left-lateral shear between indochina and south China. *Nature* 343 (6257), 431–437. doi:10.1038/343431a0

Tsuchiyama, A. (1985). Dissolution kinetics of plagioclase in the melt of the system diopside-albite-anorthite, and origin of dusty plagioclase in andesites. *Contrib. Mineral. Petr.* 89 (1), 1–16. doi:10.1007/BF01177585

Ustunisik, G., Kilinc, A., and Nielsen, R. L. (2014). New insights into the processes controlling compositional zoning in plagioclase. *Lithos* 200-201, 80–93. doi:10.1016/j.lithos.2014.03.021

Viccaro, M., Giacomoni, P. P., Ferlito, C., and Cristofolini, R. (2010). Dynamics of magma supply at Mt. Etna volcano (Southern Italy) as revealed by textural and compositional features of plagioclase phenocrysts. *Lithos* 116 (1-2), 77–91. doi:10.1016/j.lithos.2009.12.012

Wan, X., Yang, Y. Z., Li, S. Q., and Chen, F. K. (2018). Zircon U-Pb Ages, Geochemistry and Sr-Nd-Pb isotope characteristics of Menglian granites and their dark enclaves in Tengchong block of western Yunnan, China. *J. Earth Sci. Environ.* 40 (5), 563–581. (in Chinese with English abstract).

Wang, Y. (1999). Tectonic settings of late cenozoic volcanism in tibet and Tengchong area, geological review. 45 (A1), 905–913. (in Chinese with English abstract).

Winther, K. T. (1996). An experimentally based model for the origin of tonalitic and trondhjemitic melts. *Chem. Geol.* 127 (1-3), 43–59. doi:10.1016/0009-2541(95)00087-9

Wolf, M. B., and Wyllie, P. J. (1994). Dehydration-melting of amphibolite at 10 kbar; the effects of temperature and time. *Contrib. Mineral. Petr.* 115 (4), 369–383. doi:10.1007/BF00320972

Xu, Y., Li, X. L., and Wang, S. (2017). Crustal thickness and Poisson's ratio of the Tengchong volcanic area in southwestern China. *Chin. J. Geophys.* 60 (6), 2256–2264. (in Chinese with English abstract). doi:10.6038/cjg20170618

Yamamoto, T. (2007). A rhyolite to dacite sequence of volcanism directly from the heated lower crust: Late Pleistocene to Holocene Numazawa volcano, NE

Japan. *J. Volcanol. Geotherm. Res.* 167 (1-4), 119–133. doi:10.1016/j.jvolgeores.2007.05.011

Yang, W. C., Hou, Z. Z., and Yu, C. Q. (2015). 3D crustal density structure of West Yunnan and its tectonic implications. *Chin. J. Geophys.* 58 (11), 3902–3916. (in Chinese with English abstract). doi:10.6038/cjg20151102

Yao, X., Zhang, H., Wu, Z. H., Chen, G. Y., Tian, S. M., and Huang, L. (2016). Geochemical evidence of the Pliocene bimodel volcanic rocks in Yingjiang area of western Yunnan Province and its tectonic significance. *Geol. Bull. China.* 35 (8), 1346–1356. (in Chinese with English abstract).

Yu, H. M., Xu, J. D., Lin, C. Y., Pan, B., Zhao, B., Lin, X. D., et al. (2012). Microstructural characteristics of trachyandesite lavas in Heikongshan, Ma'anshan and Dayingshan volcanoes, Tengchong, Yunnan Province and its volcanological implications. *Acta Petrol* 28 (4), 1205–1216. (in Chinese with English abstract).

Yu, H. M., Zhao, B., Chen, Z., Wei, H., Yang, W., and Bai, X. (2022). Eruption history, petrogeochemistry, and geodynamic background of Tengchong volcanoes in Yunnan Province, SW China. *Geol. Soc. Spec. Publ.* 510 (1), 159–178. doi:10.1144/SP510-2020-45

Yu, L. (2016). *Genesis and tectonic significance of the Mesozoic granitoids in the Tengchong-Baoshan block, Sanjiang area*. Wuhan, China: China University of Geosciences. (in Chinese with English abstract).

Zhang, C. J. (2017). *A study on the lithofacies of Daliuchong volcano in Tengchong*. China Earthquake Administration: Institute of Geology. (in Chinese with English abstract).

Zhang, H., Wu, Z. H., Ye, P. S., Chen, G. Y., Tian, S. M., and Yao, X. (2015). The collapse of Tengchong-Gangdise Cenozoic orogenic belt and the formation of intercontinental rift: petrological records of Pliocene-Pleistocene dacite in Tengchong. *Geol. Bull. China.* 34 (1), 171–182. (in Chinese with English abstract).

Zhang, L. Y., Li, N., Zhao, Y. W., Cao, Y. Y., and Gong, L. W. (2012a). Geomorphic characteristics and fault restriction in the Tengchong volcanic region —— interpretation based on DEM and TM data. *Seismol. Geol.* 34 (4), 755–767. (in Chinese with English abstract). doi:10.3969/j.issn.0253-4967.2012.04.018

Zhang, Y. T., Liu, J. Q., and Meng, F. C. (2012b). Geochemistry of Cenozoic volcanic rocks in Tengchong, SW China: relationship with the uplift of the Tibetan Plateau. *Isl. Arc* 21 (4), 255–269. (in Chinese with English abstract). doi:10.1111/j.1440-1738.2012.00819.x

Zhao, Y. W., and Fan, Q. C. (2010). Magma origin and evolution of Maanshan volcano, Dayingshan volcano and Heikongshan volcano in Tengchong area. *Acta Petrol* 26 (4), 1133–1140. (in Chinese with English abstract).

Zhou, M. F., Robinson, P. T., Wang, C. Y., Zhao, J. H., Yan, D. P., Gao, J. F., et al. (2012). Heterogeneous mantle source and magma differentiation of quaternary arc-like volcanic rocks from Tengchong, SE margin of the Tibetan Plateau. *Contrib. Mineral. Petr.* 163 (5), 841–860. doi:10.1007/s00410-011-0702-8

Zou, H. B., Ma, M. J., Fan, Q. C., Xu, B., Li, S. Q., Zhao, Y. W., et al. (2017). Genesis and open-system evolution of Quaternary magmas beneath southeastern margin of Tibet: constraints from Sr-Nd-Pb-Hf isotope systematics. *Lithos* 272-273, 278–290. doi:10.1016/j.lithos.2016.12.012

Zou, H. B., Shen, C. C., Fan, Q. C., and Lin, K. (2014). U-series disequilibrium in young Tengchong volcanics: recycling of mature clay sediments or mudstones into the SE Tibetan mantle. *Lithos* 192-195, 132–141. doi:10.1016/j.lithos.2014.01.017